# Stepwise degradable PGA-SF core-shell electrospinning scaffold with superior tenacity in wetting regime for promoting bone regeneration

Yuan Zhang [a,1], Yutao Jian [b,1], Xiao Jiang [a,1], Xuerong Li [a,1], Xiangnan Wu [a], Juan Zhong [a], Xiaoshi Jia [a], Qiulan Li [a], Xiaodong Wang [a], Ke Zhao [a,**], Yitong Yao [a,*]

[a] Hospital of Stomatology, Guanghua School of Stomatology, Sun Yat-sen University, Guangdong Provincial Key Laboratory of Stomatology, Guangzhou, China
[b] Institute of Stomatological Research, Guangdong Provincial Key Laboratory of Stomatology, Sun Yat-sen University, Guangzhou, China

ABSTRACT

Regenerating bone in the oral and maxillofacial region is clinically challenging due to the complicated osteogenic environment and the limitation of existing bone graft materials. Constructing bone graft materials with controlled degradation and stable mechanical properties in a physiological environment is of utmost importance. In this study, we used silk fibroin (SF) and polyglycolic acid (PGA) to fabricate a coaxial PGA-SF fibrous scaffold (PGA-SF-FS) to meet demands for bone grafts. The SF shell exerted excellent osteogenic activity while protecting PGA from rapid degradation and the PGA core equipped scaffold with excellent tenacity. The experiments related to biocompatibility and osteogenesis (e.g., cell attachment, proliferation, differentiation, and mineralization) demonstrated the superior ability of PGA-SF-FS to improve cell growth and osteogenic differentiation. Furthermore, *in vivo* testing using Sprague-Dawley rat cranial defect model showed that PGA-SF-FS accelerates bone regeneration as the implantation time increases, and its stepwise degradation helps to match the remodeling kinetics of the host bone tissue. Besides, immunohistochemical staining of CD31 and Col-1 confirmed the ability of PGA-SF-FS to enhance revascularization and osteogenesis response. Our results suggest that PGA-SF-FS fully utilizing the advantages of both components, exhibits stepwise degradation and superior tenacity in wetting regime, making it a promising candidate in the treatment of bone defects.

## 1. Introduction

Oral and maxillofacial bone defects caused by disease and trauma have come to pose a global concern due to a high-morbidity, negatively affecting the life quality and causing a heavy economic burden [1]. Implantation of bone graft materials is the most commonly used therapeutic means for managing bone defects [2]. However, non-degradable bone grafts can lead to incomplete bone regeneration due to the occupation of osteogenic space and even be entirely rejected by the body [3]. Therefore, the development of degradable bone grafts becomes an essential direction for the repair of bone defects [4].

Polymers, degradable bioceramics, and magnesium metal are three types of degradable bone grafts currently used in clinical practice [5]. Polymers are available in customizable forms and have low immunogenicity and controlled degradability [6,7]. However, the release of acidic degradation products, which leads to local pH changes and poor osteoconductivity and cell adhesion, limits their use in dentistry [8,9]. In addition, the reaction between water in bone tissue and polymers leads to interphase degradation, adversely affecting the mechanical properties of the material at different hierarchical levels [10].

To address the limitations of homogeneous material, composite material can provide complementary properties and R&D ideas for biodegradable bone grafts. Polyglycolic acid (PGA) possesses good initial mechanical properties with an elastic modulus of 6 GPa - 7 GPa and 90 MPa - 100 MPa strength, markedly superior to other degradable synthetic polymers [11]. However, the PGA degrades too quickly to maintain spatial stability in the early stages of osteogenesis [12], and its

acidic intermediate products during degradation can easily induce aseptic inflammation [13,14]. Depending on its perfect biocompatibility, SF, originating from *Bombyx mori* silk, could be used in bone defect regeneration [15,16]. The tunability of the multilevel structure of SF can broaden the range of mechanical properties and degradation behavior, the complete degradation of which *in vivo* ranges from 8 weeks to more than 1 year [17]. However, it is still challenging to achieve the desired degradation and mechanical properties only by tuning the structure of SF [18]. Previous research of our laboratory group showed that SF/PGA co-mixture exhibits good osteoconductivity and histocompatibility; yet, the co-mixing treatment could not overcome the rapid degradation of PGA and the weakening effect of water molecules on the mechanical properties of PGA [19].

The nanofibrous scaffolds fabricated by electrospinning with polymer solution can largely mimic the bone matrix's structure. On this basis, coaxial-electrospinning, a flexible technique in supplying core-shell fibers, offers a unique ability to combine the best of two polymers than their single-component counterparts [20–22]. The unstable inner core is isolated by the outer shell, serving as a practicable way to minimize the chance of decomposition [23,24]. Since bone graft materials serve in an aqueous environment, the reaction between water molecules and materials leads to interphase degradation, which reduces the mechanical properties of the materials [25]. Although a number of studies have concentrated on the possible application of electrospinning scaffolds in bone defect treatment, only a few studies have elaborated on the transformation of materials in liquid environments.

In this study, we utilized coaxial electrospinning techniques to fabricate the coaxial PGA-SF-FS, hypothesized with stepwise degradation and superior tenacity in the wetting regime that can satisfy both mechanical and osteoinductive requirements for bone defect treatment. To formalize this hypothesis, we investigated the molecular mechanisms of an aqueous environment on PGA-SF-FS by molecular dynamics simulation (MDS). In addition, the morphology, mechanical properties, degradation behavior, and biological activity among PGA-SF-FS, SF fibrous scaffold (SF-FS), and PGA fibrous scaffold (PGA-FS) were characterized. We also evaluated the cytocompatibility through *in vitro* assays and histocompatibility by *in vivo* experiments.

## 2. Materials and methods

### 2.1. Fabrication of electrospinning scaffolds

#### 2.1.1. Preparation of regenerated SF

The regenerated SF was extracted from *Bombyx mori* silk (Jianai, China) according to the previously described protocol [18]. Splintered *Bombyx mori* cocoons were degummed in a boiling aqueous solution of $Na_2CO_3$ (0.02 M) for 0.5 h, rinsed thoroughly with sufficient distilled water to remove the glue-like sericin, and dried in 50 °C oven overnight. The degummed silk was dissolved in a 9.3 M LiBr solution at 60 °C for 4 h. The resulting solution was dialyzed against Milli-Q water for 3 d using a dialysis membrane (MWCO = 14,000 Da) (D9402, Sigma-Aldrich, USA) to remove LiBr ions. The SF aqueous solution was then lyophilized for 10 h to obtain regenerated SF.

#### 2.1.2. Preparation of electrospinning solution of SF and PGA

Regenerated SF was dissolved in hexafluoro-isopropanol (HFIP) (H811026, Macklin, China) at a concentration of 8% (w/v) and magnetically stirred for 12 h. PGA (Mw = 100 kDa) (06525-5, Polysciences, USA) was added to the HFIP and heated in 40 °C water bath for 3 days to prepare 10% (w/v) electrospinning solution.

#### 2.1.3. Electrospinning process

To obtain PGA-SF-FS, SF and PGA electrospinning solutions were respectively transferred into two separate syringe pumps connected to the coaxial spinneret (14 G for the outer tube and 19 G for the inner tube) and spun at an electric voltage ranging from 18 to 23 kV, set to release fluid at a rate of 3 mL/h for SF and 1 mL/h for PGA. Electrospinning of SF and PGA was performed at a flow rate of 2 mL/h under applied voltage from 10 to 15 kV through an 18 G needle. Electrospinning fibers were collected on an aluminum foil with −5 to 0 kV. Subsequently, SF-FS and PGA-SF-FS were immersed in absolute ethanol for 30 min to induce β-sheet transformation, and all fibers (SF-FS, PGA-FS, and PGA-SF-FS) were cross-linked by 1% glutaraldehyde at 30 °C water bath for 1 h.

### 2.2. Scaffold characterization

#### 2.2.1. Morphological analysis

The morphology of scaffolds was observed under a scanning electron microscope (SEM) (Phenom ProX, Phenom-World, Netherlands) at an acceleration voltage of 10–15 kV after the samples were sputter-coated with gold for 30 s. The core-shell structure of PGA-SF was characterized by transmission electron microscopy (TEM) (JEM 1400 Plus, JEOL, Japan) and SEM. The average fiber diameter was measured using Image J software (V1.51, NIH, USA) by analyzing 50 random fibers from at least 3 sites respectively on each sample (n = 3) using SEM images.

#### 2.2.2. Component analysis

The scaffold elements were detected using energy-dispersive X-ray spectroscopy (EDS) attached to the SEM and TEM. The infrared spectra of SF-FS, PGA-FS, and PGA-SF-FS in the range of 400–2000 $cm^{-1}$ were measured by attenuated total reflection-Fourier transform infrared spectroscopy (ATR-FTIR) (Nicolet iS50, Thermo Scientific, USA) at a 2 $cm^{-1}$ resolution. Each sample was cut into squares measuring $1.5 \times 1.5$ $cm^2$ before being placed on the sample holder.

#### 2.2.3. Tensile mechanical properties

Tensile tests were tested with a universal testing machine (Instron 5697, Instron, USA) in ambient atmospheric conditions at a 10 mm/min strain rate to measure Young's modulus, tensile strength, and elongation at break. The specimens were rectangular pieces (10 mm × 60 mm) in accordance with ASTM D3039 for testing methods. The dry and wet samples (by spraying 3 mL PBS on each sample to get wet) were tested using at least five replicates at 25 °C.

### 2.3. MDS analysis

Single-chain SF and PGA with polymerisation degrees of 6 and 36, respectively, were constructed using the Materials Studio (2020, Accelrys, USA) to ensure that the linear chain lengths of PGA and SF were of similar length in order to minimize the effects of different chain lengths. Subsequently, boxes containing 7 linear SF and 10 linear PGA with a 0.8 $g/cm^3$ density were built using the amorphous cell module. In addition, the PGA and SF structures were merged using the Build Layers tool to obtain PGA-SF layered composite polymers. In order to investigate the effect of polymer water on PGA-SF, 45 wt% water was inserted into the polymer boxes using the Monte Carlo algorithm of the Adsorption module. Once the polymer molecular model was constructed, the polymer structure was first structurally optimized by the Forcite module using the COMPASS force field, followed by 100 ps molecular dynamics simulations under the constant-energy, constant-volume ensemble (NVT) to relax the structure. Subsequently, structural and property simulations were performed using LAMMPS software (2023 version) with ReaxFF reactive force field. Structural optimisation was first carried out with convergent force and energy tolerances of $10^{-5}$ Kcal/(mol-Å) and $10^{-5}$ kcal/mol, respectively. Then, molecular dynamics simulations for structural relaxation were carried out for 100 ps under the constant-temperature, constant-pressure ensemble (NPT) system at 300 K and 0 periostatic pressure. Finally, uniaxial tensile simulations were performed under the NPT tether. The tensile strain rate was $10^{-6}$/fs. During the tensile process, the box side was kept at 0-periapsis to account for the Poisson effect of the polymer material. The

simulation step size was 0.25 fs.

### 2.4. In vitro degradation

For assessment of scaffold degradation, four rectangular samples ($21.6 \pm 1.2$ mg) for each group were immersed in PBS solution (pH = 7.4) for a period of 0, 4, 8, 12, and 16 w at 37 °C. The weight loss in mass of the scaffold was obtained with the following equation (1):

$$\text{Weight loss (\%)} = \frac{W_0 - W_d}{W_0} \times 100\% \qquad (1)$$

where $W_0$ is the initial weight, and $W_d$ is the dry weight after degradation.

A pH meter replaced PBS every third day following pH value measurement (S220–K, Mettler, Switzerland). The surface morphology of scaffolds after degradation was observed under SEM, and chemical analysis was performed using FTIR-ATR as mentioned before.

### 2.5. Simulated body fluid (SBF) immersing test

For bioactivity evaluation, scaffolds were cut to size 15 mm in diameter and 200 μm in thickness (n = 4) and immersed in SBF (CC024, M&C Gene Technology, China) at 37 °C water bath. The specimens at predetermined times up to 14 and 28 d were removed from the fluid, rinsed with deionized water, and lyophilized for 10 h. The morphology and composition were characterized by SEM and EDS, respectively.

### 2.6. In vitro experiments

#### 2.6.1. Cell culture

Prior to cell seeding, scaffolds were immersed in 75% ethanol for 2 h, washed with PBS twice, and sterilized with UV light for 2 h. The bone marrow mesenchymal stem cells (BMSCs) were isolated from the tibiae of 4-week-old Sprague-Dawley (SD) rats. The primary BMSCs were cultured in low-glucose type Dulbecco's modified Eagle's medium (L-DMEM) (C11885500BT, Gibco, USA) supplemented with 10% fetal bovine serum (FBS) (04-400-1A, Biological Industries, Israel) and 1% penicillin/streptomycin in a humidified atmosphere containing 5% $CO_2$/95% air at 37 °C.

BMSCs of passage 3 were used for the subsequent experiments. Cells were seeded on the scaffolds at $1 \times 10^5$ cells/mL or $1 \times 10^6$ cells/mL when performing reverse transcription-quantitative polymerase chain reaction (qRT-PCR). For the alkaline phosphatase (ALP) activity test, Alizarin Red staining (ARS), and qRT-PCR, osteogenic differentiation medium (RAXMX-90021, Cyagen, China) was used for cell osteogenic differentiation after 3 days incubation period by L-DMEM.

#### 2.6.2. Cell morphology

To observe attachment morphologies of BMSCs after 1, 4 and 7 d culture, cells were fixed in 4% paraformaldehyde (PFA) for 1 h and permeabilized with 0.5% Triton X-100 for 10 min. Actin-Tracker Green (C22015, Beyotime, China) was diluted in a solution containing 0.1% Triton X-100 and 2.5 mg/mL bovine serum albumin (BSA) (SRE0096-50g, Sigma-Aldrich, New Zealand) at a 1:100 ratio, and each well was treated with 200 μL diluted Actin-Tracker Green with overnight incubation at 4 °C in a light-avoidant environment. Cell nuclei were stained with 4′,6-diamidino-2-phenylindole (DAPI) (C1005, Beyotime, China) for 5 min at room temperature. Next, the morphologies were visualized by laser scanning confocal microscope (FV3000, Olympus, Japan) (n = 3).

#### 2.6.3. Cell proliferation

DNA quantification assay was used to evaluate cell proliferation at 1, 4, and 7 d by Quant-iT™ PicoGreen® dsDNA reagent kits (P11496, Invitrogen, USA) (n = 3). The fluorescence was read in a microplate

reader (Synergy H1, Biotek, USA) at 485/535 nm. DNA standard curve was prepared to determine the DNA concentration of the sample.

#### 2.6.4. Osteogenic differentiation

Osteogenesis was evaluated using the ALP activity test and ARS. After 7 and 14 d osteogenic differentiation, cell-scaffold constructs were homogenized in 400 μL assay buffer using a homogenizer for 3 min on ice. The solution was then centrifuged at 1200 g for 15 min at 4 °C to remove insoluble materials. Then, the supernatant was collected and tested with an ALP assay kit (ab83369, Abcam, UK) (n = 3). The absorbance at 405 nm was determined using a microplate reader.

After 14 and 21 d osteogenic differentiation, scaffolds were fixed in 4% PFA at room temperature for 30 min and then washed 3 times by PBS. Next, each well was stained with 100 μL ARS solution (ALIR-10001, Cyagen, China) for 10 min, and scaffolds were visualized with an upright fluorescence microscope (BX63, OLYMPUS, Japan). Calcium nodules were quantified by 10% cetylpyridinium chloride, which was dissolved in 10 mM sodium phosphate at room temperature for 15 min (n = 3). The absorbance at 405 nm was determined using a microplate reader.

RT-qPCR was used to assess the expression of osteogenic marker genes of the cells seeded on the SF-FS, PGA-FS, and PGA-SF-FS, including ALP, Col-1, OCN, Osterix (OSX), and Runx2 after 14 d osteogenic differentiation, and GAPDH was used as housekeeping gene (n = 3). Cells seeding on SF-FS served as the control group, providing a baseline standard for comparison with PGA-SF-FS. Total RNA was extracted using an RNA-Quick Purification Kit (RN001, ES Science, China) and converted to cDNA (RR036A, Takara, Japan). The expression of osteogenic marker genes was stained with Hieff® qPCR SYBR Master Mix (No Rox) (H2302190, Yeasen Biotechnology, China) and detected by LightCycler®96 system (LC96, Roche, Switzerland). The synthesized primers are listed in Table 1.

### 2.7. In vivo experiments

#### 2.7.1. Surgery procedure

To evaluate the effects of PGA-SF-FS on bone regeneration in the cranial bone defects, sixty 6-week-old SD rats (220–250 g) were randomly divided into four groups (n = 5/group): SF-FS, PGA-FS, PGA-SF-FS, and control groups (n = 5). All the animals were housed in an environment with a temperature of $22 \pm 1$ °C, a relative humidity of $50 \pm 1\%$, and a light/dark cycle of 12/12 h. All animal studies (including the rat euthanasia procedure) were done in compliance with the regulations and guidelines of Sun Yat-sen University institutional animal care and conducted according to the AAALAC and the IACUC guidelines (Approval no: SYSU-IACUC-2022-000674).

Briefly, SD rats were administered anesthesia through intraperitoneal injection of 1% sodium pentobarbital (50 mg/kg). A round full-thickness defect with a diameter of 8 mm was carefully created on the calvarium, and then scaffolds were placed into it, except for the control group. The incisions were closed with a 4 - 0 resorbable suture. In order to prevent infection, penicillin (400000 U/kg/d) was administered via intramuscular injection for 3 d following surgery. At 4, 8, and 12 w post-implantation, rats were euthanized with overdose pentobarbital injection, and the harvested specimens were collected and fixed in 4% paraformaldehyde for subsequent examination.

**Table 1**
Primers used in qRT-PCR.

| Gene | Forward primer sequence (5′-3′) | Reverse primer sequence (5′-3′) |
| --- | --- | --- |
| ALP | GGAACGGATCTCGGGGTACA | ATGACCTTGAACCGGGACCA |
| Col-1 | AGGAAGGAGTAGGATTGGAGGT | AGGTCTGGAGTAAAGGGCAC |
| Osterix | GTTCACCTGTCTGCTCTGCT | TTGGCTTCTTCTTCCCCGAC |
| OCN | GCATCTATGGCACCACCGTT | GCCTTCTCCAACCCCTACCA |
| Runx 2 | CACAAGTGCGGTGCAAACTT | AATGACTCGGTTGGTCTCGG |
| GAPDH | AGTGCCAGCCTCGTCTCATA | GATGGTGATGGGTTTCCCGT |

Micro-CT analysis evaluated bone formation using a micro-CT imaging system (μCT50, SCANCO, Switzerland) at 70 kV and 200 μA, with a scanning resolution of 10 μm. The scaffolds-implanted regions were scanned and reconstructed using μCT Scan Program (v6.1, SCANCO, Switzerland), and the bone volume/total volume (BV/TV) was calculated. To characterize general morphology, the specimens after micro-CT scanning were decalcified, dehydrated, paraffin-embedded, and sliced into 5 μm sections. The histological sections stained with Hematoxylin-Eosin (HE) and Masson's Trichrome (MT) were then mounted on glass slides. Immunohistochemical (IHC) staining of Col-1 was performed to assess the extracellular matrix of newly formed bone. IHC staining of CD31 was performed to characterize the vascularization dynamics of newly formed bone. The digital images of histological sections were analyzed and captured under a digital slide scanner (Aperio AT2, Leica, Germany).

### 2.8. Statistical analysis

Statistical analysis was conducted using SPSS Statistics (25.0, IBM, USA). One-way ANOVA followed by Games-Howell or Kruskal-Wallis was used to analyze differences among groups, depending on whether data followed normality and homogeneity of variance requirements. The graphing was performed using Origin (2022, OriginLab Corporation, USA) with a bar plot shown with mean ± standard deviation. Differences were considered significant only if the $p < 0.05$ (* indicates $p < 0.05$, ** indicates $p < 0.01$, *** indicates $p < 0.001$).

## 3. Results

### 3.1. Characterization of PGA-SF-FS

The morphology of SF-FS, PGA-FS, and PGA-SF-FS observed by SEM and corresponding diameter distributions are shown in Fig. 1A. SF-FS, PGA-FS, and PGA-SF-FS with relatively smooth surfaces were randomly distributed without beaded structures. The average diameter of SF-FS, PGA-FS and PGA-SF-FS were 1.98 ± 0.44 μm, 0.94 ± 0.19 μm, and 2.09 ± 0.44 μm, respectively. SF-FS was similar to PGA-SF-FS in diameter ($p > 0.05$), while PGA-FS corresponded to the inner core diameter of PGA-SF-FS ($p > 0.05$). The EDS spectrum (Table 2) showed that the atomic percentage (C, N, and O elements) of PGA-SF-FS was basically identical to SF-FS, while no N element could be detected on PGA-FS.

**Table 2**
EDS spectrum obtained from the outermost layer of SF-FS, PGA-FS, and PGA-SF-FS.

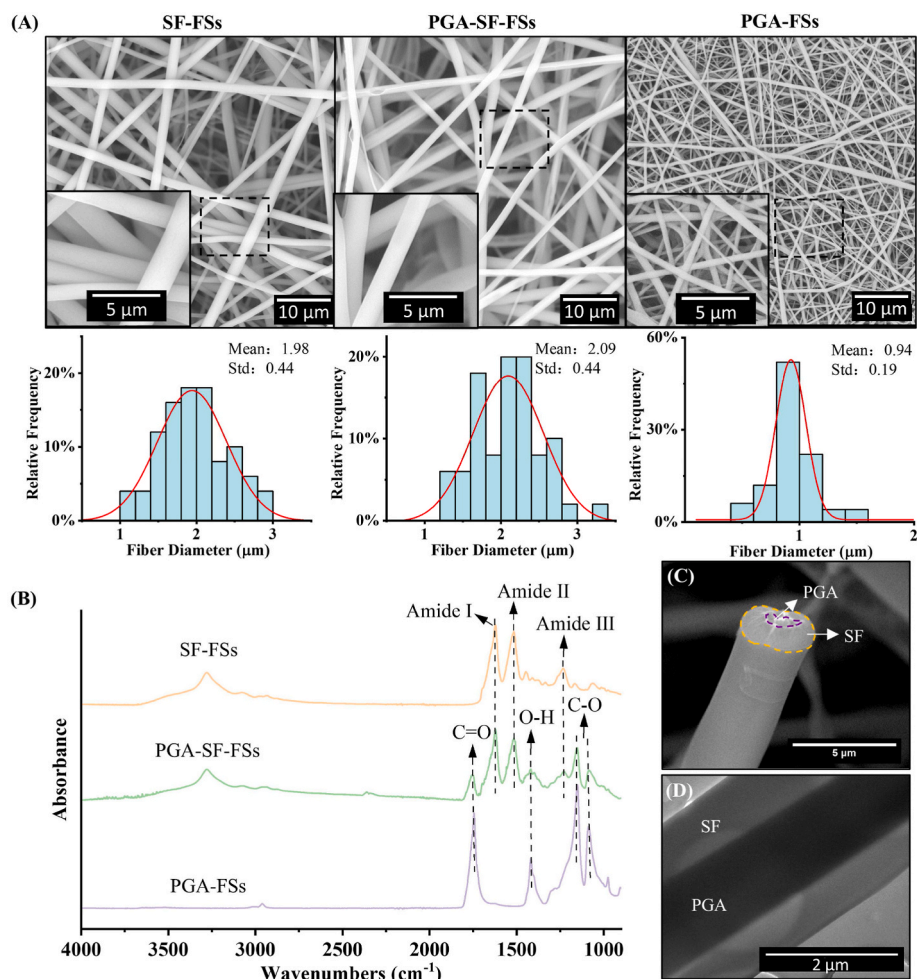| Scaffold | Atomic percentage (%) | | |
|---|---|---|---|
| | C | N | O |
| SF-FS | 33.22 | 37.66 | 29.12 |
| PGA-SF-FS | 35.07 | 34.53 | 30.40 |
| PGA-FS | 53.86 | – | 46.14 |



**Fig. 1. Characterization of the morphology and composition of SF-FS, PGA-FS and PGA-SF-FS. (A)** SEM images and histograms of fiber diameter distributions of SF-FS, PGA-FS, and PGA-SF-FS (scale bar: 10 μm for low magnification and 5 μm for high magnification). **(B)** FTIR spectra of SF-FS, PGA-FS, and PGA-SF-FS. **(C)** SEM image of PGA-SF-FS fracture surface (scale bar: 5 μm). **(D)** TEM image of PGA-SF-FS (scale bar: 2 μm).

FTIR spectra of SF-FS, PGA-FS, and PGA-SF-FS are shown in Fig. 1B. PGA-SF-FS and SF-FS showed characteristic peaks at 1626 cm$^{-1}$, 1518 cm$^{-1}$, and 1228 cm$^{-1}$. PGA-SF-FS showed characteristic peaks at 1081 cm$^{-1}$, 1148 cm$^{-1}$, 1417 cm$^{-1}$, and 1752 cm$^{-1}$ when compared with PGA-FS. SEM images of the section and TEM patterns of PGA-SF-FS with smooth surface and fine limit are shown in Fig. 1C and D.

### 3.2. Tensile mechanical properties

To investigate the feasibility of scaffolds in bone defect reparation, tensile mechanical properties of SF-FS, PGA-FS, and PGA-SF-FS were characterized in dry and wet conditions. Elongation at break, tensile strength, and Young's modulus based on the stress-strain curves are illustrated in Fig. 2 and Table 3.

Under dry conditions, PGA-FS showcased a remarkable elongation at break, which was significantly higher than SF-FS and PGA-SF-FS (all $p <$ 0.01), and PGA-SF-FS was also higher than that of SF-FS ($p <$ 0.01). In addition, PGA-SF-FS demonstrated superior tensile strength, which was notably higher than that of SF-FS ($p <$ 0.001) and PGA-FS ($p <$ 0.05); also, PGA-FS exhibited an intermediate but significant improvement over SF-FS ($p <$ 0.05). Young's Modulus of SF-FS was significantly

**Table 3**
Tensile mechanical properties of SF-FS, PGA-FS and PGA-SF-FS.

| Condition | Scaffold | Elongation at break (%) | Tensile strength (MPa) | Young's modulus (MPa) |
|---|---|---|---|---|
| Dry | SF-FS | 0.77 ± 0.27 | 1.68 ± 0.57 | 267.39 ± 83.97 |
| | PGA-SF-FS | 5.52 ± 0.60 | 5.34 ± 1.16 | 157.15 ± 42.65 |
| | PGA-FS | 72.52 ± 6.54 | 3.36 ± 0.03 | 108.91 ± 2.95 |
| Wet | SF-FS | 51.77 ± 12.48 | 0.91 ± 0.03 | 14.67 ± 5.99 |
| | PGA-SF-FS | 110.07 ± 14.25 | 3.11 ± 0.49 | 54.19 ± 7.70 |
| | PGA-FS | 85.91 ± 9.06 | 2.94 ± 0.21 | 84.21 ± 7.14 |

higher than that of PGA-FS ($p <$ 0.05), but no significant difference was observed when comparing SF-FS and PGA-SF-FS ($p >$ 0.05).

Under wet conditions, PGA-SF-FS exhibited the highest elongation at break, significantly surpassing both PGA-FS ($p <$ 0.05) and SF-FS ($p <$ 0.001), and PGA-FS displayed a significantly higher elongation at break than SF-FS ($p <$ 0.05). Moreover, PGA-SF-FS and PGA-FS showed no significant difference in tensile strength ($p >$ 0.05), both significantly higher than SF-FS ($p <$ 0.001). The Young's modulus of PGA-FS was significantly higher than that of PGA-SF-FS ($p <$ 0.01), and both PGA-SF-
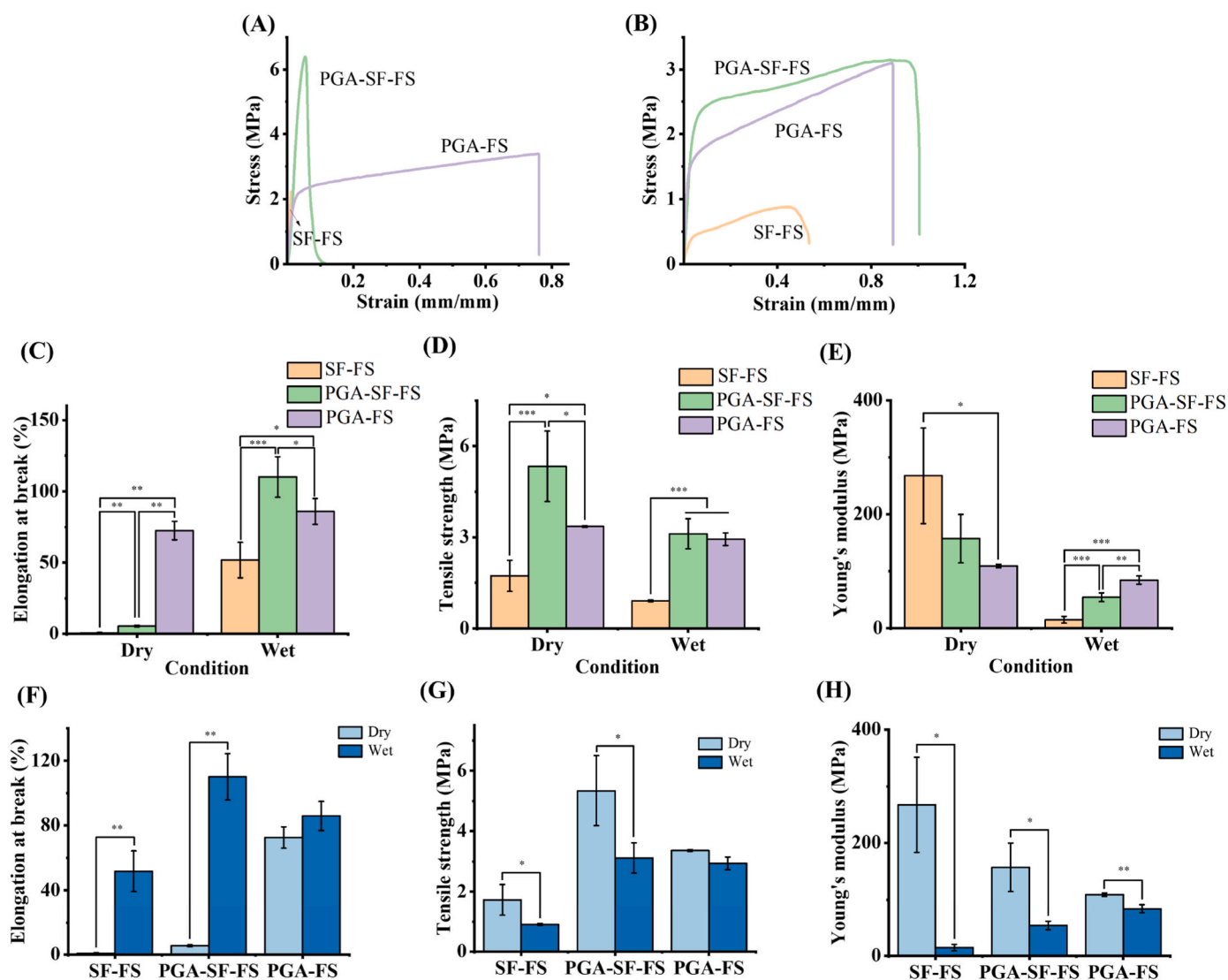


**Fig. 2. Tensile mechanical property analysis of SF-FS, PGA-FS and PGA-SF-FS in dry and wet conditions. (A, B)** Representative tensile stress-strain curves in dry (A) and wet conditions (B). **(C, F)** Elongation at break in dry and wet conditions. **(D, G)** Tensile strength in dry and wet conditions. **(E, H)** Young's modulus in dry and wet conditions. *$p <$ 0.05, **$p <$ 0.01, ***$p <$ 0.001.

FS and PGA-FS were significantly higher than SF-FS (all $p < 0.001$).

Compared to the dry state, all three groups exhibited a significant decrease in Young's modulus under wet conditions ($p < 0.05$ for both SF-FS and PGA-SF-FS; $p < 0.01$ for PGA). Both SF-FS and PGA-SF-FS demonstrated a significant increase in elongation at break under wet conditions ($p < 0.01$), while PGA-FS showed no significant change ($p > 0.05$). Both PGA-SF-FS and SF-FS had a significant reduction in tensile strength under wet conditions (all $p < 0.05$), while PGA-FS exhibited no significant change ($p > 0.05$).

### 3.3. MDS analysis

Molecular structures of SF, PGA-SF, and PGA were examined under dry and hydrated conditions (Fig. 3). The 45% water content introduction resulted in uniform water infiltration within SF, PGA-SF, and PGA. Notably, PGA-SF layered composite polymer exhibited robust interlayer binding in dry and hydrated conditions. During uniaxial tensile simulations, the PGA-SF composite polymer maintained excellent interlayer cohesion, while SF, especially in the presence of water, exhibited noticeable collapsing perpendicular to the direction of stretching. PGA was stretched along the stretching direction and showed similar structural changes under dry and wet conditions.

During uniaxial tensile testing, the total bond energy of SF, PGA-SF, and PGA under dry and 45% water conditions was investigated (Fig. 4A). Under dry conditions, there was no significant change in total bond energy with increasing strain for SF, PGA-SF, and PGA. In the presence of 45% water, total bond energy increased with strain for all three polymers. Notably, PGA-SF exhibited a significantly greater increase compared to SF and PGA. Beyond a 0.5 m/m strain, PGA demonstrated a pronounced and rapid increase in total bond energy, while SF exhibited relatively stable behavior.

The evolution of hydrogen bond energy in SF, PGA-SF, and PGA under dry and 45% water conditions during uniaxial tensile testing was also examined (Fig. 4B). Under dry conditions, no significant change in hydrogen bond energy was observed for SF, PGA-SF, and PGA with increasing strain. In the presence of 45% water, hydrogen bond energy increased with strain for all polymers. Like total bond energy, PGA-SF displayed a notably larger increase compared to SF and PGA, while SF

and PGA exhibited similar trends without significant differences.

### 3.4. In vitro degradation

SF-FS, PGA-FS, and PGA-SF-FS were immersed in PBS solution for 16 w to assess the *in vitro* degradation. As shown by the photograph and SEM characterization (Fig. 5), SF-FS and PGA-SF-FS kept relatively intact fibrous structures during 16 w degradation; however, PGA-FS degraded into fragments and powder after 4 w. PGA-SF-FS showed an increase in surface roughness and the appearance of cracks over time. Following the cracking of the SF shell and exposure of the PGA core, the diameter distribution of PGA-SF-FS gradually expanded after 8 w. In contrast, the SF-FS showed well-defined, smooth fibers that kept a constant diameter during 16-w immersion.

PGA-SF-FS showed relatively quick weight loss (21.75 ± 1.14%) in the first 8 w and maintained a slow ascent to 24.77 ± 0.35% at 16 w (Fig. 6A). PGA-FS degraded thoroughly after 4 w, while weight loss of SF-FS during 16 w could be negligible.

After 1 w of degradation, the pH of PGA-SF-FS decreased to approximately 6.0 and gradually stabilized at around 6.5. However, the pH value of PGA-FS dropped sharply to 3.74 within 2 w and then gradually increased to above 6.0 after 6 w. The pH of SF-FS kept steady at around 7.0 during 16 w degradation (Fig. 6B).

The FTIR spectra shown in Fig. 6C indicate that all PGA-SF-FS samples had the characteristic peaks at 1626 cm$^{-1}$, 1518 cm$^{-1}$, 1228 cm$^{-1}$, 1081 cm$^{-1}$, 1148 cm$^{-1}$, 1417 cm$^{-1}$, and 1752 cm$^{-1}$ during 16 w degradation. All peaks declined from 8 w but were still visible until 16 w; yet a decline for 1626 cm$^{-1}$, 1518 cm$^{-1}$, and 1228 cm$^{-1}$ was slower.

### 3.5. SBF immersing test

This test investigated the mineralization behavior of SF-FS, PGA-FS, and PGA-SF-FS during 4 w immersion in SBF. As shown in Fig. 7, SEM images and EDS spectrum revealed small particles containing Ca and P elements, adhering to the fiber surfaces of both SF-FS and PGA-SF-FS after 2 weeks. The calculated Ca/P ratios for the surface deposits on SF-FS and PGA-SF-FS were 0.61 and 1.17, respectively. After 4 weeks,
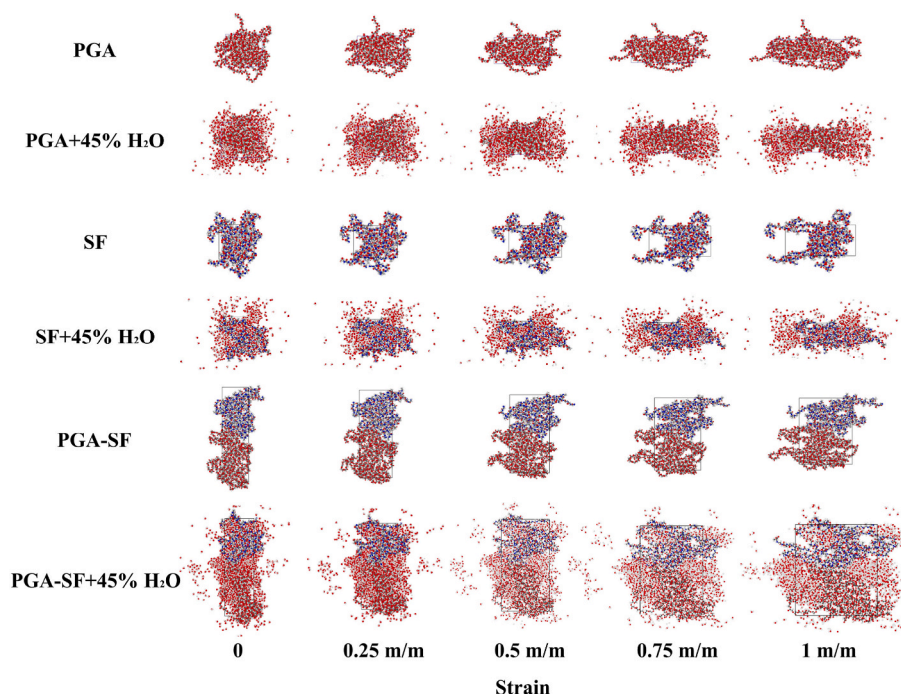


**Fig. 3.** Molecular structure simulation of SF, PGA and PGA-SF layered composite polymers under dry and hydrated conditions at uniaxial stress.
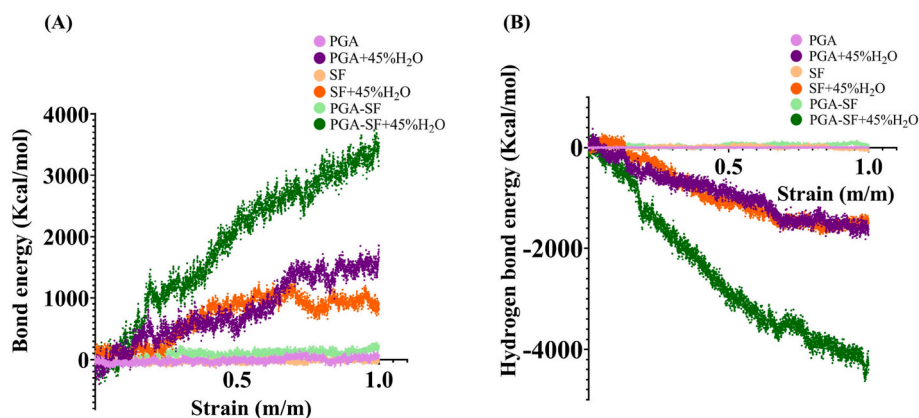
**(A)**



**(B)**

**Fig. 4. Bond energy evolution during uniaxial tensile test simulation. (A)** Total bond energy change. **(B)** Hydrogen bond energy change.

both SF-FS and PGA-SF-FS exhibited well-defined and regularly shaped spherical deposits surrounding the fibers, while more fused and stacked spherical deposits were found in PGA-SF-FS. At higher magnification, images revealed crystal protrusions on the surface of the spherical deposits. At this stage, the Ca/P ratios for the deposits on SF-FS and PGA-SF-FS surfaces were 1.8 and 1.61, respectively. Since PGA-FS degraded and was hard to observe, no images were shown for this group.

### 3.6. In vitro cell studies

#### 3.6.1. Cell attachment

The adhesion and morphological responses of BMSCs cultured on SF-FS, PGA-FS, and PGA-SF-FS are shown in Fig. 8A. After 1 day of culture, BMSCs on SF-FS and PGA-SF-FS displayed round-shaped nuclei with elongated cytoplasm. Also, cells on both SF-FS and PGA-SF-FS exhibited extensive spreading, displaying chromatic particles and a mesh-like cytoskeletal structure within the cytoplasm. In contrast, BMSCs on partially fused PGA fibers exhibited round or irregular shapes and displayed deformed nuclei, condensation, and deficiency of cytoplasmic contents.

On the 4th and 7th d, the number of BMSCs on SF-FS increased significantly, and the cells showed elongated shapes. The cytoplasm displayed more distinct chromatic particles and a well-defined cytoskeletal framework. Similarly, cells on PGA-SF-FS showed a noticeable increase in cell quantity, with enhanced adhesion and spreading. The cytoskeletal structure was more abundant and clear, aligned along the direction of cell extension, and accompanied by numerous chromatic particles within the cytoplasm. In contrast, the number of cells on PGA-FS decreased, and the cells exhibited irregular morphologies with spiky protrusions, cytoplasmic condensation, discontinuous membrane, and the absence of a prominent cytoskeletal structure.

#### 3.6.2. Cell proliferation

Fig. 8B shows no significant differences in cell quantity among the three groups on the first day of culture ($p > 0.05$). By the 4th day, a similar cell number was seen for both SF-FS and PGA-SF-FS ($p > 0.05$), but also a higher cell number compared to PGA-FS (all $p < 0.05$). A similar trend was followed after 7 days of culture, and the gap between SF-FS or PGA-SF-FS and PGA-FS increased.

#### 3.6.3. Osteogenic differentiation

ALP activity of cells after 7 and 14 d osteogenic differentiation on SF-FS, PGA-FS, and PGA-SF-FS are shown in Fig. 9B. After 7 and 14 days of culture, there was no significant difference in ALP activity between SF-FS and PGA-SF-FS (all $p > 0.05$). However, both SF-FS and PGA-SF-FS exhibited significantly higher ALP activity than the PGA-FS (all $p < 0.05$). Although ALP expression showed no significant difference between SF-FS and PGA-SF-FS ($p > 0.05$), the comparable expression levels

indicate sustained osteogenic differentiation potential on both materials.

As shown in Fig. 9C, at day 14, osteogenic markers were significantly upregulated on PGA-SF-FS compared to SF-FS. Specifically, the expression levels of *Runx2, OCN,* and *Col-1* genes were significantly higher on PGA-SF-FS than on SF-FS (*Runx2, OCN, and Col-1*: $p < 0.001$; *OSX*: $p < 0.01$). Due to the rapid degradation of PGA-FS, insufficient sample quantities were collected; therefore, the results for PGA-FS were not presented.

Alizarin Red staining of cells after 14 and 21 d osteogenic differentiation on SF-FS, PGA-FS and PGA-SF-FS are shown in Fig. 9A. At 14 d, circular calcium nodules were observed on both SF-FS and PGA-SF-FS, with some nodules showing signs of fusion. On PGA-FS surfaces, irregularly shaped calcium nodules were observed, with some appearing elliptical or spindle-shaped. Notably, partial degradation and detachment of PGA-FS were observed (indicated by red arrows in Fig. 9A), where no calcium nodules were evident. By 21 d, the calcium nodules on SF-FS and PGA-SF-FS surfaces exhibited an increased staining area. In contrast, PGA-FS showed fragmentation, with no distinct calcium nodules observed. Quantitative analysis of calcium nodule formation (Fig. 9D) at 14 d indicated no significant difference between SF-FS and PGA-SF-FS ($p > 0.05$), but both were significantly higher than PGA-FS (all $p < 0.001$). At 21 d, PGA-SF-FS demonstrated a slight increase compared to SF ($p < 0.05$), and both SF-FS and PGA-SF-FS were significantly higher than PGA-FS (all $p < 0.001$).

### 3.7. In vivo animal experiments

All the rats survived during and after surgery, and no signs of inflammatory reactions and fractures were observed at the site of the bone defect. At 4, 8, and 12 w, defect sites implanted with SF-FS and PGA-SF-FS looked opaque and firm to the naked eye. In contrast, PGA-FS and the blank control group showed relative transparency, with only a thin layer of connective tissue covering the surface of the cranial defect (Fig. 10A).

A 3D reconstruction based on micro-CT scans illustrated the differences in bone formation at the defect sites (Fig. 10B). At 4 w, the SF-FS group displayed scattered new bone at the defect edge with little sparse trabeculae extending towards the center. The PGA-SF-FS group exhibited edge and central new bone, with denser and more extensive trabeculae. By 8 weeks, the SF group demonstrated increased new bone extending towards the defect center, while the PGA-SF-FS group showed a more merged and denser new bone structure than SF-FS. At 12 w, the SF-FS group exhibited a larger and denser new bone area compared with that at 8 w, with distinguishable defect boundaries. PGA-SF-FS group showcased a nearly complete filling of the defect area with integrated new bone, and the boundary became less distinct. In contrast, PGA-FS and the blank control group showed minimal new bone, mainly at the defect edges, throughout the whole period of 12 weeks.
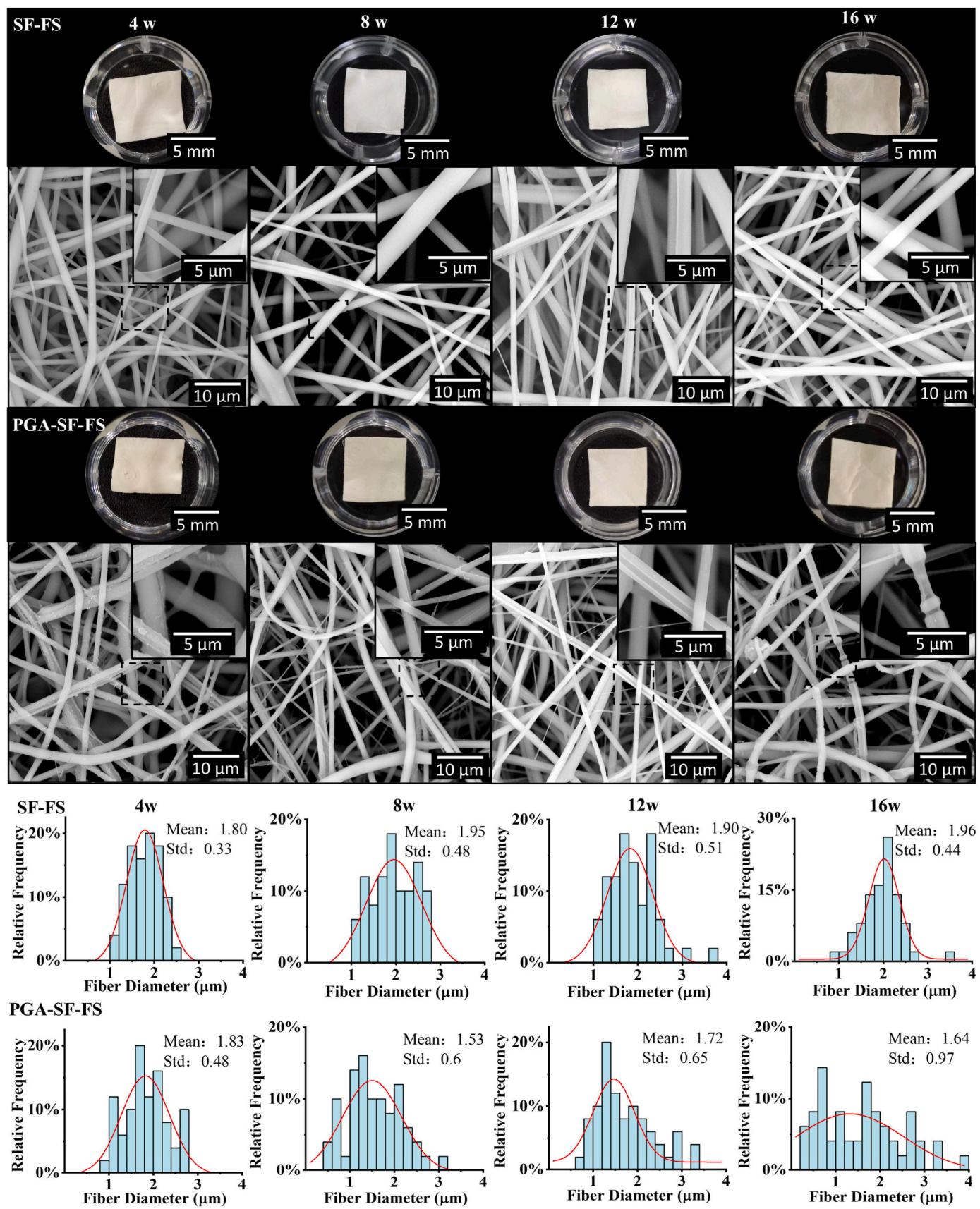
**Fig. 5.** Morphological change and fiber diameter distributions of SF-FS, PGA-FS, and PGA-SF-FS incubated in PBS solution at 37 °C after 4, 8, 12, and 16 w (scale bar: 5 mm for photographs, 10 μm for SEM images at low magnification and 5 μm for SEM images at high magnification).
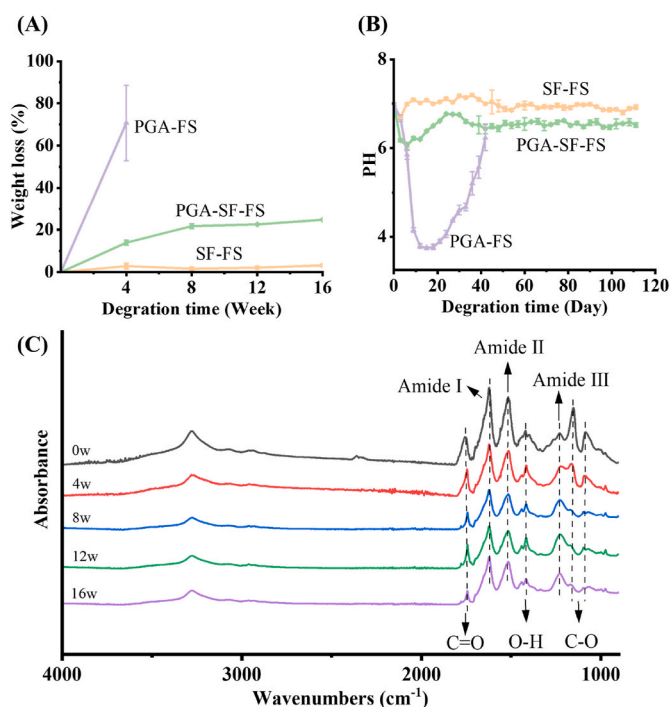
**Fig. 6.** Degradation of SF-FS, PGA-FS, and PGA-SF-FS after incubation in PBS for 0–16 w. **(A)** Percentage of weight loss of SF-FS, PGA-FS, and PGA-SF-FS during 16 w degradation. **(B)** The pH of degradation solution of SF-FS, PGA-FS, and PGA-SF-FS during 16 w degradation. **(C)** FTIR absorption spectra of PGA-SF-FS from 0 to 16 w degradation.

BV/TV of the defect zone from 4 to 12 w is shown in Fig. 11A and C. As for SF-FS, BV/TV increased gradually over 4, 8, and 12 weeks, reaching $4.84 \pm 1.3\%$, $8.84 \pm 1.2\%$, and $11.66 \pm 1.4\%$, respectively. A significant improvement was observed at 8 weeks compared to 4 weeks ($p < 0.01$) and at 12 weeks compared to 8 weeks ($p < 0.05$). PGA-SF-FS group showed a significant increase from 4 to 8 weeks ($p < 0.05$) and remained stable between 8 and 12 weeks ($p > 0.05$), with values of $6.29 \pm 2.16\%$, $13.93 \pm 2.81\%$, and $13.83 \pm 4.05\%$, respectively. BV/TV of PGA-FS changed insignificantly over time, with values of $2.96 \pm 2.31\%$, $5.83 \pm 1.8\%$, and $5.05 \pm 4.31\%$ at 4, 8, and 12 weeks ($p > 0.05$), respectively. BV/TV of the control group increased slightly from $2.55 \pm 0.93\%$ at 4 weeks to $5.95 \pm 1.53\%$ at 8 weeks ($p < 0.05$) but showed no significant change after 8 weeks ($p > 0.05$). At 4 weeks, no significant differences were observed among groups ($p > 0.103$). At 8 weeks, PGA-SF-FS showed superior results compared to PGA-FS and control group ($p < 0.001$) and significantly higher than SF-FS ($p < 0.05$), while no significant difference was observed between PGA-FS and blank control ($p > 0.05$). At 12 weeks, PGA-SF-FS exhibited the highest BV/TV, significantly surpassing both PGA-FS, blank control ($p < 0.001$), and SF-FS ($p < 0.05$), while no significant difference was observed between PGA-FS and blank control ($p > 0.05$).

The trabecular number (Tb·N) of the defect zone from 4 to 12 w are shown in Fig. 11B and D and. Tb.N of SF-FS were $0.43 \pm 0.06$/mm, $0.81 \pm 0.29$/mm, and $1.02 \pm 0.24$/mm at 4, 8, and 12 w, respectively. There was no significant difference between 4 and 8 weeks ($p > 0.05$), but Tb·N at 12 w significantly increased compared to 4 w ($p < 0.05$). Tb.N of PGA-SF-FS were $0.47 \pm 0.07$/mm, $1.78 \pm 0.44$/mm, and $1.16 \pm 0.28$/mm at 4, 8, and 12 w, respectively. There was a significant increase in Tb·N at 8 w compared to 4 w ($p < 0.01$), but no significant change was observed after 8 w ($p > 0.05$). Tb.N of PGA-FS was significantly higher at 8 weeks compared to 4 w and 12 w ($p < 0.05$). No significant change of Tb·N in the control group was observed from 4 to 12 w ($p > 0.05$). At 4 w, no significant difference was observed between SF-FS and PGA-SF-FS ($p > 0.05$), but both were significantly higher than PGA-FS ($p < 0.05$). At 8 weeks, PGA-SF-FS exhibited the highest Tb·N, significantly surpassing SF-FS, PGA-FS ($p < 0.01$), and the control group ($p < 0.001$). At 12 w, there was no significant difference between SF-FS and PGA-SF-FS ($p > 0.05$), but both were significantly higher than PGA-FS and the control
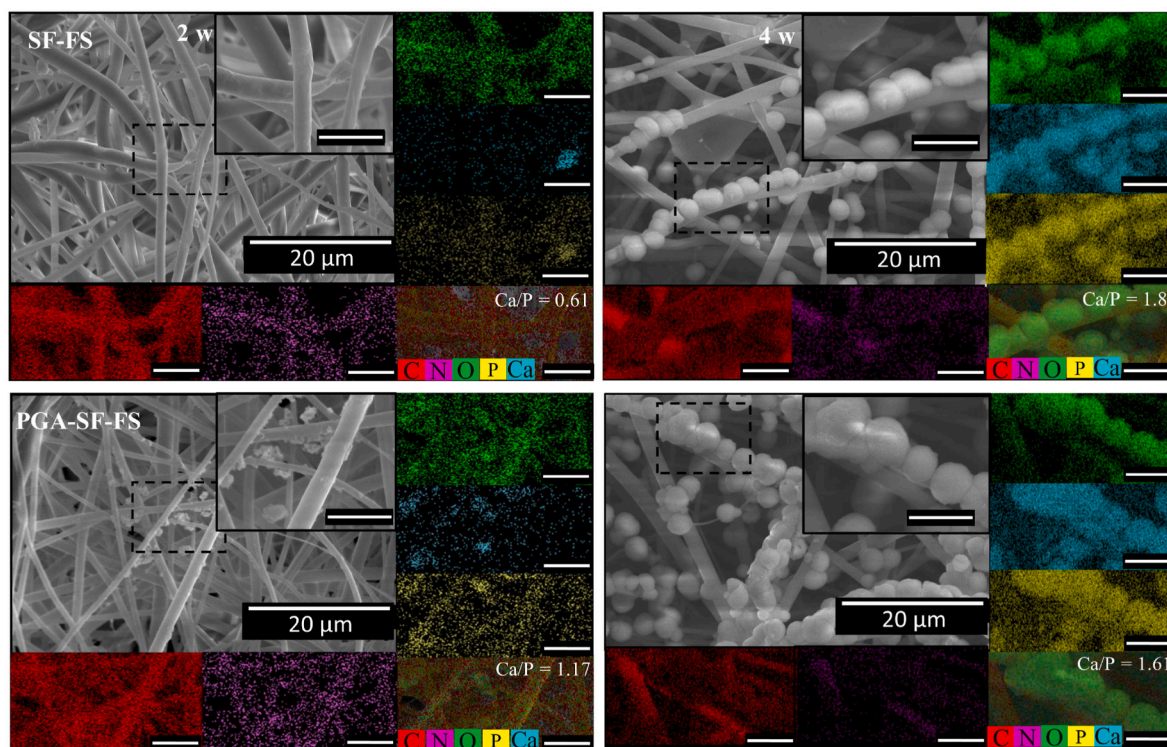


**Fig. 7.** SEM micrographs and the corresponding EDS elemental mapping images of the prepared SF-FS and PGA-SF-FS (scale bar: 20 μm for low magnification and 5 μm for high magnification).
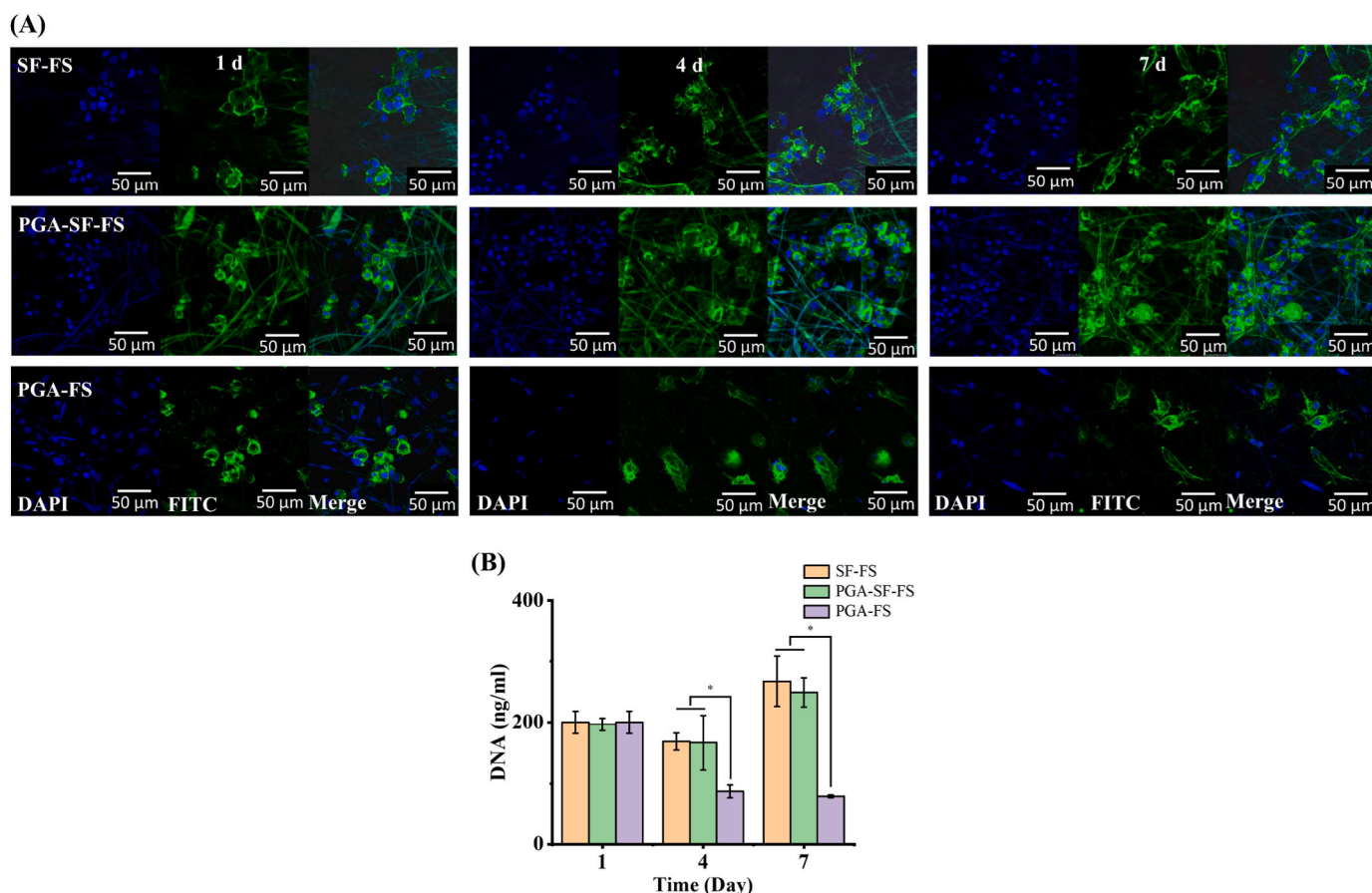
**(A)**



**(B)**



**Fig. 8.** **BMSCs attachment and proliferation during 7 d culture on SF-FS, PGA-FS, and PGA-SF-FS.** **(A)** Fluorescent micrographs of BMSCs on SF-FS, PGA-FS, and PGA-SF-FS after 1, 4, and 7 d culture (scale bar: 50 μm). **(B)** DNA quantification assay after 1, 4, and 7 d culture. $*p < 0.05$.

group ($p < 0.01$), while PGA-FS and the control group showed no significant difference ($p > 0.05$).

Fig. 12 shows the HE staining of sections collected at 4, 8, and 12 weeks. Both SF-FS and PGA-SF-FS exhibited new bone formation within the defect area. The newly generated bone had a comparable color and density to the host bone. In contrast, the PGA-FS was completely degraded. The PGA-FS and control groups showed limited new bone trabeculae localized around the defect periphery. At 4 w, the SF-FS and PGA-SF-FS groups displayed new bone primarily near the defect edges, with clear demarcation between the implanted material and the newly formed bone. At 8 w, new bone with rich vascularization was observed near the edges and center of the defects in the PGA-SF-FS group. At 12 w, defects implanted with PGA-SF-FS exhibited seamless integration between the newly formed bone and the existing bone tissue, with no apparent boundary. New bone almost filled the bone defect, with minimal material residue observed. In contrast, defects implanted with SF-FS still contained non-ossified regions, and the implanted scaffold material persisted within the new bone, accompanied by evident fibrous material yet to degrade.

Fig. 13 shows the MT staining of sections collected at 4, 8, and 12 weeks. In both SF-FS and PGA-SF-FS groups, the area of new bone gradually increased from the defect margins to the center. Matured bone tissues stained in red were mainly located at the newly formed bone in PGA-SF-FS since 4 w. After 12 w, the defect implanted with PGA-SF-FS consisted mainly of mature red-stained bone tissue, with light blue staining at the center. In contrast, the SF-FS groups showed numerous lightly stained blue collagen fibers and undegraded scaffold materials. The defects implanted with PGA-FS and the control group were predominantly filled with loosely stained light blue connective tissue from 4 to 12 weeks.

The results of CD31 immunohistochemical staining are shown in Fig. 14, which aimed to characterize the vascularization dynamics. After implantation of PGA-SF-FS into the defect for 4 w, CD31 expression was observed mainly in the new bone and scaffolds near the defect margin, and some CD31 expression was also observed in the center of the defect. At 8 w, CD31 expression was increased at the edge and in the center of the defect, around the new bone and extending into the bone matrix. At 12 w, the bone defect was largely filled with dense, mature bone tissue, and CD31 expression was predominantly observed in the connective tissue surrounding the bone, with comparatively less expression within the bone tissue.

From 4 to 8 weeks, CD31 expression in the defect implanted with SF-FS was primarily concentrated in the newly formed bone at the defect margin and in the material surrounding the new bone. In addition, limited CD31 expression was observed in the scaffolds in the center of the defect at 8 weeks; however, it was not until 12 weeks that more significant CD31 expression was observed in the center of the defect. Significantly, CD31 expression was observed in the connective tissue of both the PGA-FS and control groups from 4 to 12 weeks.

Fig. 15 shows the immunohistochemical staining results of Col-1. Col-1 expression was observed in defects implanted with PGA-SF-FS from 4 to 8 weeks and distributed around the newly formed bone, in the bone matrix, within bone lacunae, and the scaffold material surrounding the bone periphery. Twelve weeks after the implantation, Col-1 expression was observed in the newly formed bone and the connective tissue surrounding the bone periphery. In the defects implanted with SF-FS, Col-1 expression was primarily observed around the newly formed bone at the defect edge, with little expression within the bone lacunae of the newly formed bone and the scaffold material at the central defect. From 8 to 12 weeks, Col-1 expression was seen in the newly formed bone
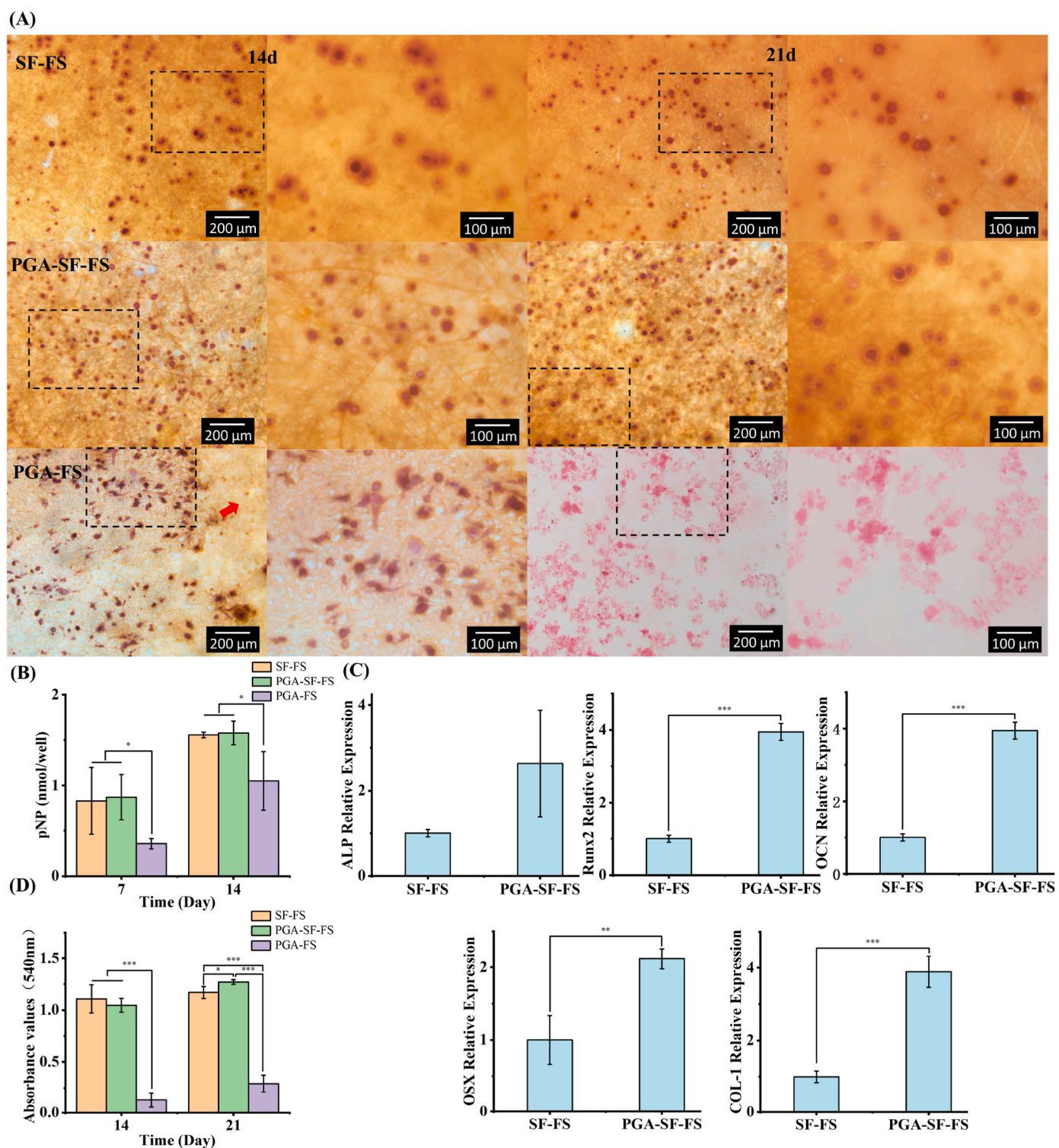
**Fig. 9. Osteogenic differentiation of BMSCs on SF-FS, PGA-FS and PGA-SF-FS. (A, D)** ARS and quantitative analysis of the calcium nodules on SF-FS, PGA-FS and PGA-SF-FS after 14 and 21 d osteogenic differentiation. The red arrow indicates PGA-FS desquamation with cell reduction due to the rapid degradation of PGA-FS. (scale bar: 200 μm for low magnification and 100 μm for high magnification). **(B)** ALP activity of cells after 7 and 14 d osteogenic differentiation on SF-FS, PGA-FS and PGA-SF-FS. **(C)** Relative expression of osteoblast-specific genes of BMSCs seeding on SF-FS and PGA-SF-FS after 14 d osteogenic differentiation. *$p < 0.05$, **$p < 0.01$, ***$p < 0.001$. (For interpretation of the references to colour in this figure legend, the reader is referred to the Web version of this article.)

at the central defect. In contrast, defects implanted with PGA-FS and the control group showed predominantly Col-1 expression in the connective tissue at the defect edge, with rare expression at the central defect.

## 4. Discussion

This study focused on the fabrication and characterization of PGA-SF core-shell fibrous scaffolds from macro and micro perspectives, presenting improved tenacious, degradative, and biocompatible properties
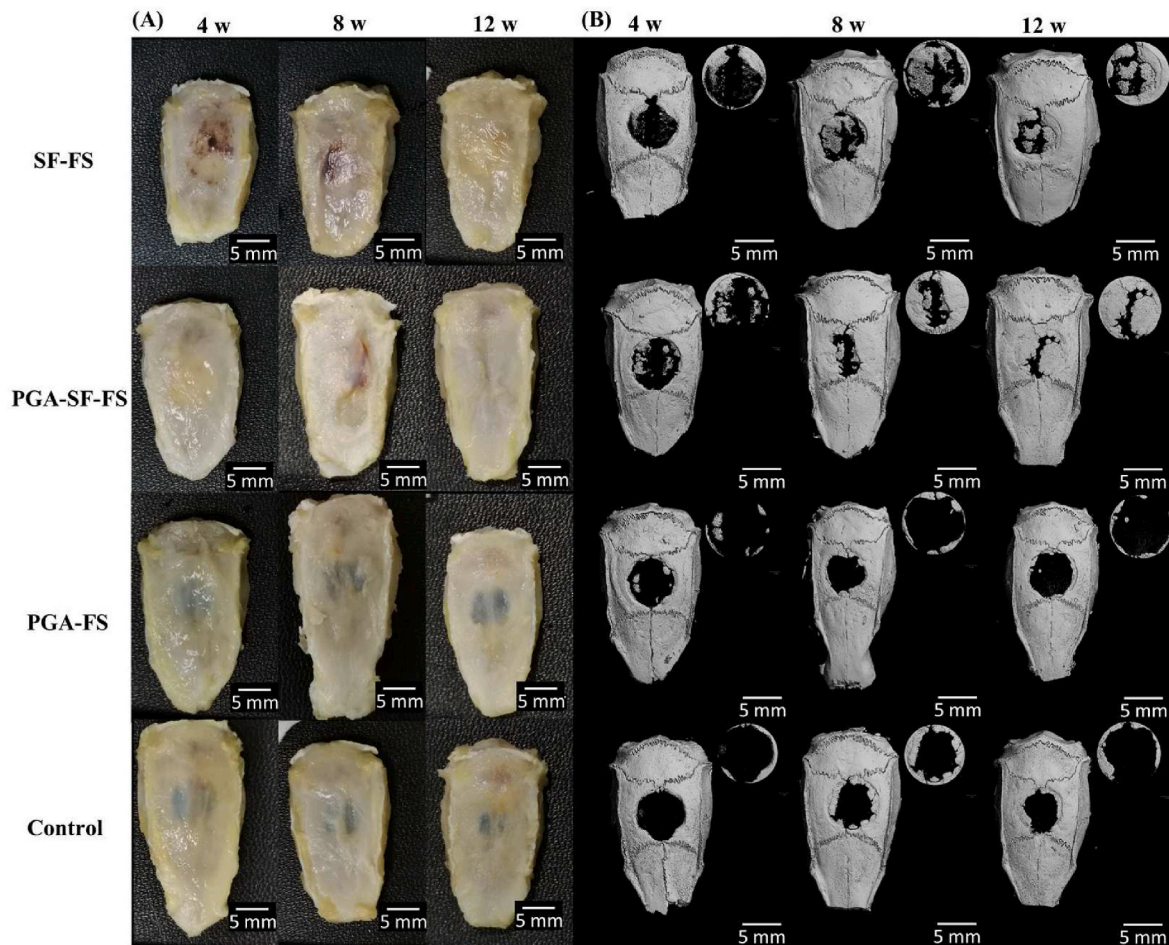
**Fig. 10.** Bone regeneration of SF-FS, PGA-FS, PGA-SF-FS and control groups in critical cranial defects after 4, 8, and 12 w. **(A)** Specimen photographs (scale bar: 5 mm). **(B)** A 3D reconstruction of cranial defects (scale bar: 5 mm).

for application in bone defect repair. Nanofibers, which mimic the architecture of bone matrix, provide superior sites for cell attachment and highly penetrating pores for cell migration and show great potential for bone tissue engineering [26].

The internal core-shell structures of PGA-SF-FS were verified by clear boundaries using TEM, stratified section morphology using SEM, and characteristic element content using the EDS spectrum [27]. The FTIR spectra indicated that SF-FS and PGA-SF-FS maintained the typical $\beta$-sheet structure, which was confirmed by the presence of the typical $\beta$-sheet bands of the amide I (1626 cm$^{-1}$), amide II (1518 cm$^{-1}$), and amide III (1228 cm$^{-1}$) [28]. PGA-FS and PGA-SF-FS showed strong peaks of C–O and C=O at 1148 cm$^{-1}$ and 1752 cm$^{-1}$, respectively, and weak peaks at 1081 cm$^{-1}$, confirming the bulk presence of C–O groups. Besides, the absorption peak of PGA-FS and PGA-SF-FS at 1417 cm$^{-1}$ corresponded to the O–H group [29]. The typical PGA peaks corresponding to the PGA-SF-FS weaken significantly, although there was no change in the positions, mainly due to the encapsulation and protection of the core-shell structure. Also, no reaction occurred between the shell and core in PGA-SF-FS.

The core-shell fibers are considered a polymer-polymer composite. The material used as the core usually possesses favorable mechanical properties for reinforcing core-shell composites [30]. In this study, we chose a tensile experiment to characterize the mechanical properties of scaffolds because the structure and character of electrospinning fibers are similar to the organic matrix of bone, which is mainly subjected to tensile stresses [7]. We found that SF-FS exhibited brittleness and rigidity in dry conditions and softness in wet conditions. PGA-FS were ductile and flexible both in dry and wet conditions. PGA-SF-FS exhibited

the highest tensile strength in dry conditions, likely due to the tenacity of PGA-FS, which, to some extent, prevented excessive elongation of SF-FS, thereby increasing the overall tensile strength. In addition, the properties of the surface and interface are also vital for mechanical performance. The MDS results indicated that the interface between PGA and SF in PGA-SF-FS was well integrated during the stretching process. Non-covalent interactions were formed between the inner core and outer shell, thus diminishing the core-shell interface and forming an integral hierarchical fiber [31]. This combination of good interfaces may also help improve the overall strength of the materials. In wet conditions, the energy of the hydrogen bond and the total bond at the PGA-SF interface increased gradually with strain, which suggested that in a wet environment, hydrogen bonding interactions at the interface are strengthened under strain, providing additional toughness to the whole material. This also explained why PGA-SF-FS has a higher elongation at break and satisfied tensile strength in the wet state. Besides, water molecules could enhance chain mobility in the amorphous regions of SF, increasing flexibility and plasticity and reducing brittleness [32]. Brittle materials with low elongation at break often lack the mechanical properties required for bone substitutes [33]. Excellent tensile strength and elongation at break in the moist environment of physiological fluids allow for flexibility during physiological movements or minor deformations [34]. Young's modulus dropped to varying degrees in three groups, indicating that water had a negative effect on mechanical properties, especially on SF-FS, which is because water weakens the strength of $\beta$-sheet crystallite, thus determining the strength of silk [35].

Previous experimental studies showed that the cytoskeleton of BMSCs on the tenacious surface spreads better than on soft surfaces [36].
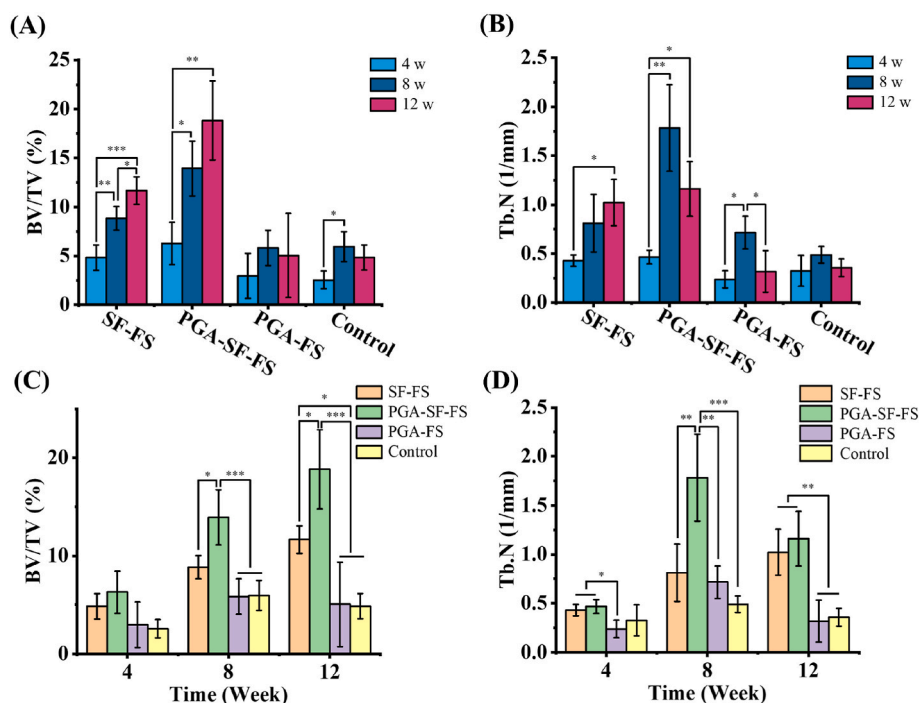
**Fig. 11.** Microcomputed tomographical analysis of new bone formed in calvarial defect after SF-FS, PGA-FS and PGA-SF-FS implantation for 4–12 w. **(A, C)** Bone volume/total volume of defect zone. **(B, D)** A trabecular number of the defect zone. *p < 0.05, **p < 0.01, ***$p < 0.001$.

Reduced cell spreading and increased motility have been reported on softer, less stiff substrates. In contrast, cells exert larger traction forces, create more stable focal adhesions, and form more defined actin stress fibers on substrates with higher strength. The mechanical microenvironment of scaffolds also greatly influences the differentiation of BMSCs, which tends to differentiate into bone on tenacious surfaces [37]. Despite a noticeable increase in elongation to break, excessive loss in strength and modulus of SF-FS in wet cannot meet the requirements of bone regeneration. PGA, a synthetic polymer of classic polyester with good mechanical properties, can keep its elasticity and strength in wet conditions before hydrolyzing. Accordingly, the combination of SF and PGA brought self-adaptive tensile properties to PGA-SF-FS. PGA-SF-FS had excellent strength in dry conditions and maintained strength and modulus of entire fibers with brilliance to present performance in elongation in wet conditions.

The pH of the degradation solution of PGA-SF-FS dropped to nearly 6.0 after 1 w, which may be attributed to the hydrolysis of a few PGA fibers that lacked SF shells. The pH of PGA-SF-FS showed a slight decrease and remained around 6.5 after 4 w. The mild pH decrease of PGA-SF-FS was likely related to the small amounts of cracks and breaks in the SF shell, which led to the degradation of PGA. The pH decrease of PGA-SF-FS was significantly lower than that of pure PGA-FS, indicating that the encapsulation of SF greatly prevents the degradation of PGA. The cracks that occurred in the SF shell were more obvious in PGA-SF-FS (occurred from 4 to 16 w) than pure SF-FS (occurred in 16 w), which may be because the core-shell structure of PGA-SF-FS weakened the thickness of SF layer compared to pure SF-FS. Overall, most of the fibers kept integrity to provide necessary support and a neutral environment for osteogenesis, which could be verified by pH, FTIR and SEM. Also, the cracks of some core-shell fibers may result in lager pores, which may benefit the movement of cells and substance transportation [38].

According to previous studies, pure SF-FS exhibit little change throughout the 16 weeks of immersion in PBS [39–41]. *In vivo*, SF is entirely degraded by proteases within a year, which is longer than required for bone tissue repair [42]. On the contrary, PGA degrades much faster, leading to a severe weakening of its mechanical properties. The strength of PGA decreases by about half after 2 w *in vivo* and almost

to zero after 4 w [43]. In PGA-SF-FS, the characteristic peaks of PGA gradually decreased over 8–16 weeks, and they even persisted at 16 weeks, which suggested a sustained, controlled, and slower degradation process of the PGA core. The characteristic peaks of the SF shell also diminished at 8w, revealing a more moderate decline. Our results showed that the combination of SF and PGA in the form of core-shell modulated the degradation behavior of both. The degradation rate of PGA was slowed down by the protection of SF shell when SF seemed to be accelerated by PGA core in PGA-SF-FS. The possible mechanisms of stepwise degradation of PGA-SF-FS are as follows:

Firstly, SF is degraded by surface corrosion, with mass loss starting from the interface in contact with water and propagating to the center [44], whereas PGA is degraded by bulk erosion, resulting in fragile materials with impaired mechanical properties and functions [45]. The core-shell structure can protect the PGA core from over-rapid degradation, benefiting from its stable frame, which is not easily deformed during bulk erosion. Secondly, the ester bond structure and small methylene groups of PGA are unstable and susceptible to hydrolytic attack [46]. Hydrolysis cleaves the ester bonds in the amorphous polymer matrix, causing PGA degradation to occur primarily in the amorphous region. After dissolving the amorphous region, the exposed ester bonds in the crystalline region become susceptible to hydrolysis, ultimately leading to the dissolution of the polymer chain. The wrapping of SF around PGA reduces the exposure of ester bonds in the amorphous region, thus delaying the degradation of PGA. Thirdly, it should be noted that the glass transition temperature ($T_g$) of PGA is relatively low, ranging from 35 °C to 45 °C [47]. After implantation, the high concentration of water in the polymer can cause the $T_g$ to drop below the physiological temperature [48]. When the surrounding temperature exceeds the $T_g$, the amorphous portion of the PGA shifts from a frozen to a thawed state, and the amorphous region transforms into a rubbery state, which facilitates the entry of water molecules and accelerates degradation. The $T_g$ of SF (220 °C [49]) is significantly higher than that of PGA. By wrapping SF around PGA, the $T_g$ of PGA-SF-FS can be increased, which reduces the stretching of molecular chains within the system at *in vivo* temperature. This also reduces the exposure of ester bonds in the amorphous region of PGA, thereby slowing down the
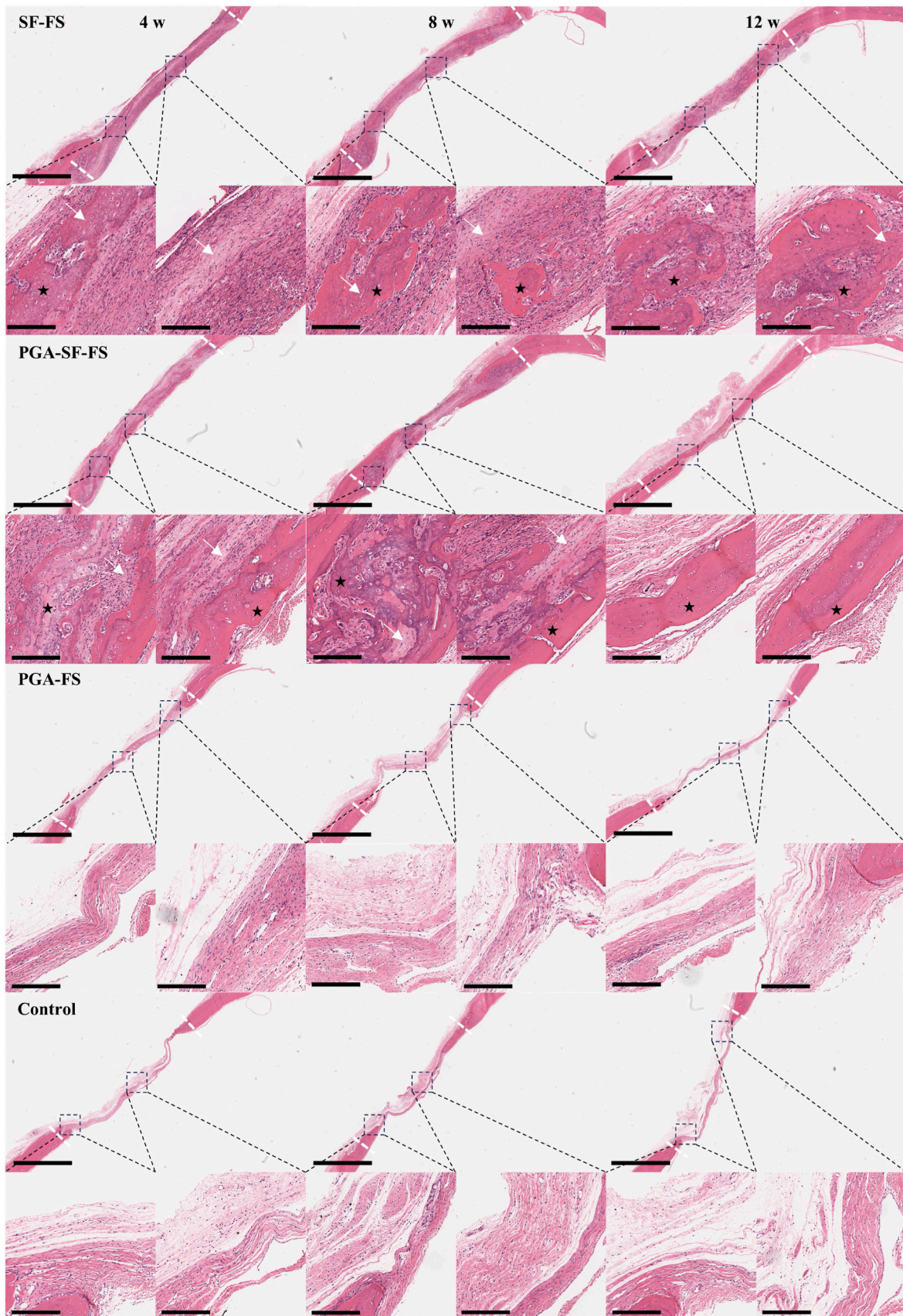
**Fig. 12. Histological images after HE staining of SF-FS, PGA-FS, PGA-SF-FS and control groups implanted in the cranial defect for 4, 8, and 12 w.** A white dashed line represents the defect margin, white arrows indicate scaffolds, and pentacle represents the new bone (scale bar: 2 mm for low magnification and 200 μm for high magnification).
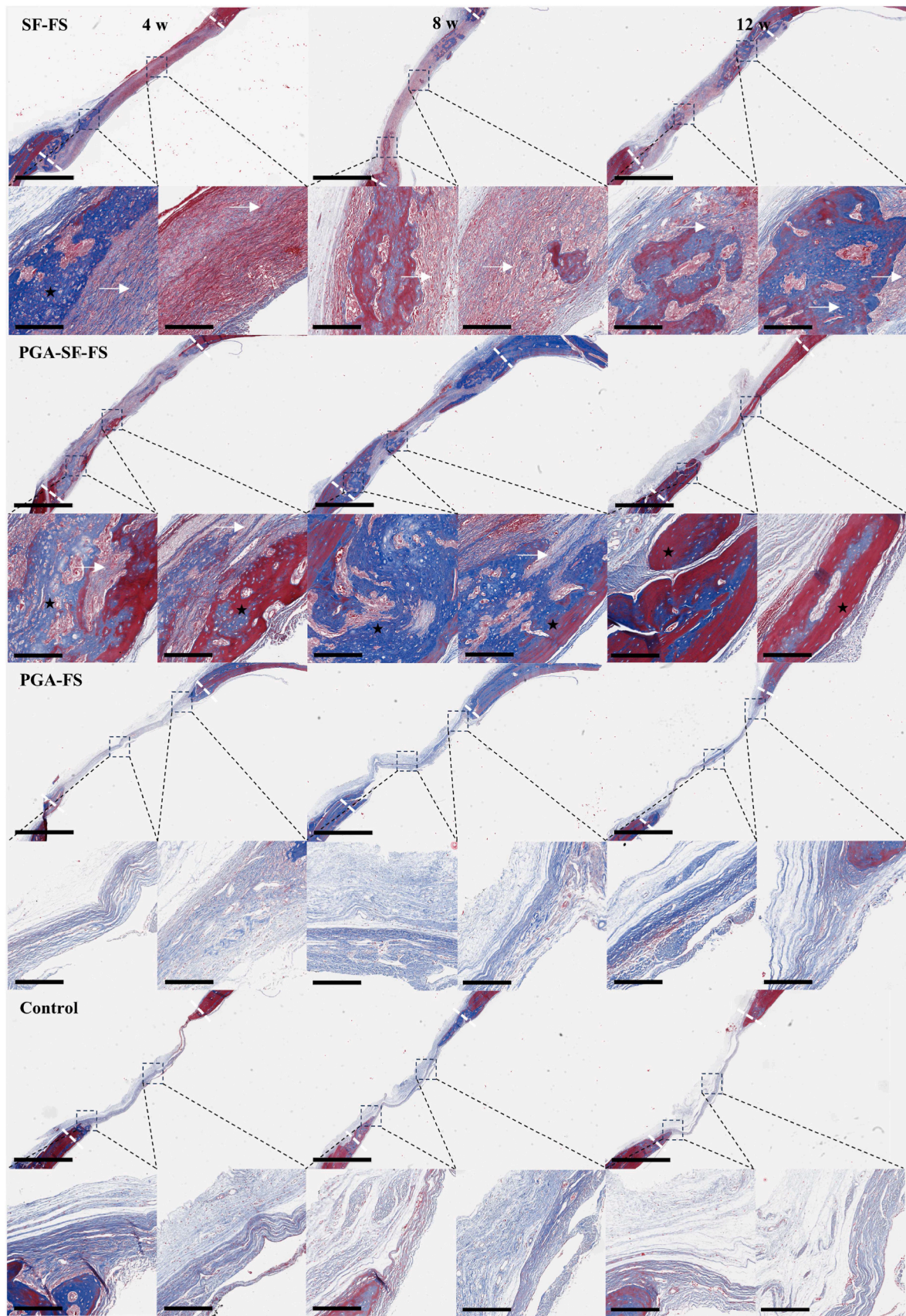
**Fig. 13. Histological images after MT staining of SF-FS, PGA-FS, PGA-SF-FS and control groups implanted in the calvarium defect for 4, 8 and 12 w.** The white dashed line represents a defect margin, the white arrows indicate residual scaffolds, and pentacle represents new bone (scale bar: 2 mm for low magnification and 200 μm for high magnification).
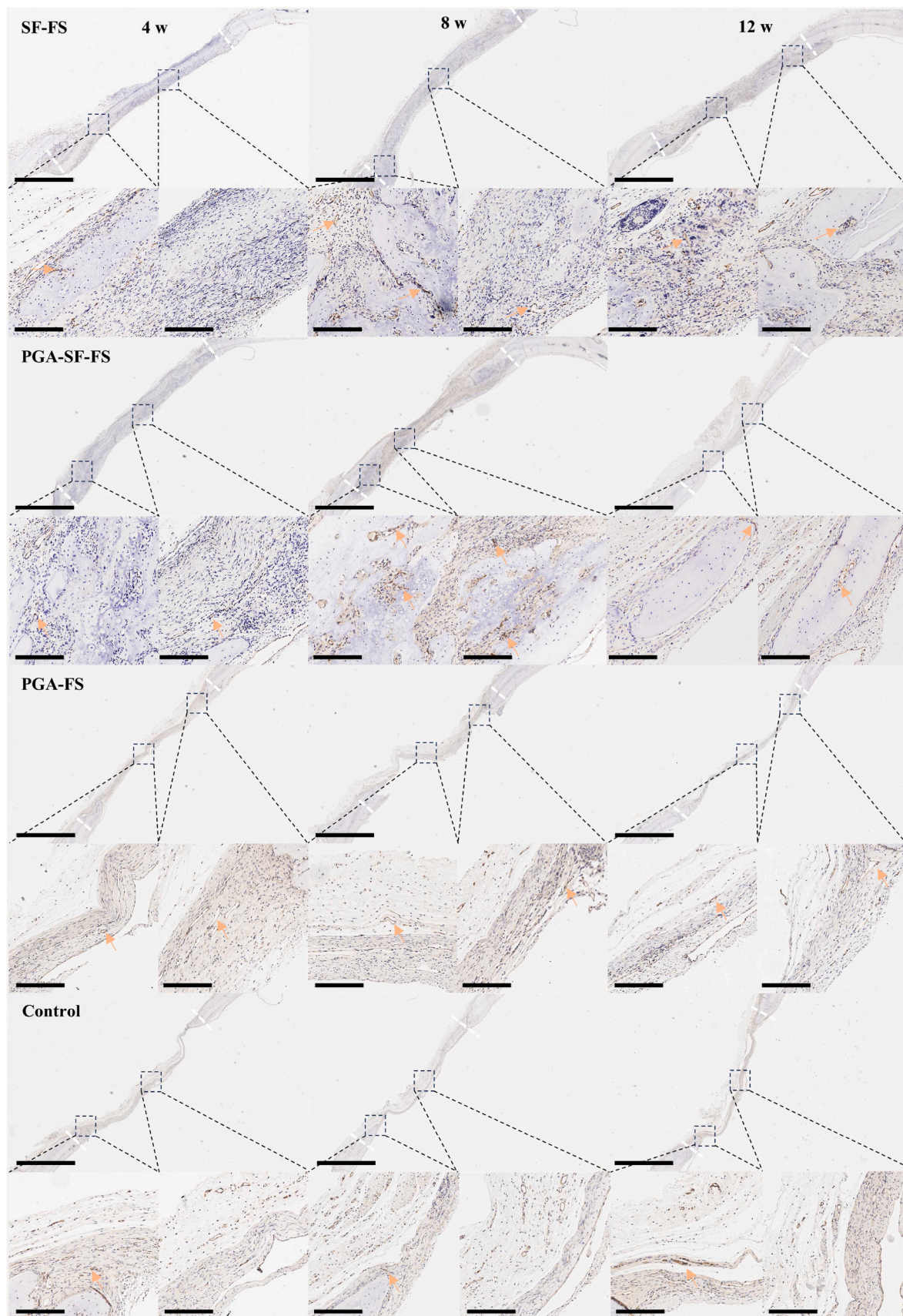
**Fig. 14. CD31 immunohistochemical staining of SF-FS, PGA-FS, PGA-SF-FS, and control groups implanted in the calvarium defect for 4, 8, and 12 w.** The white dashed line represents the defect margin, and the orange arrows represent the CD31 expression (scale bar: 2 mm for low magnification and 200 μm for high magnification). (For interpretation of the references to colour in this figure legend, the reader is referred to the Web version of this article.)
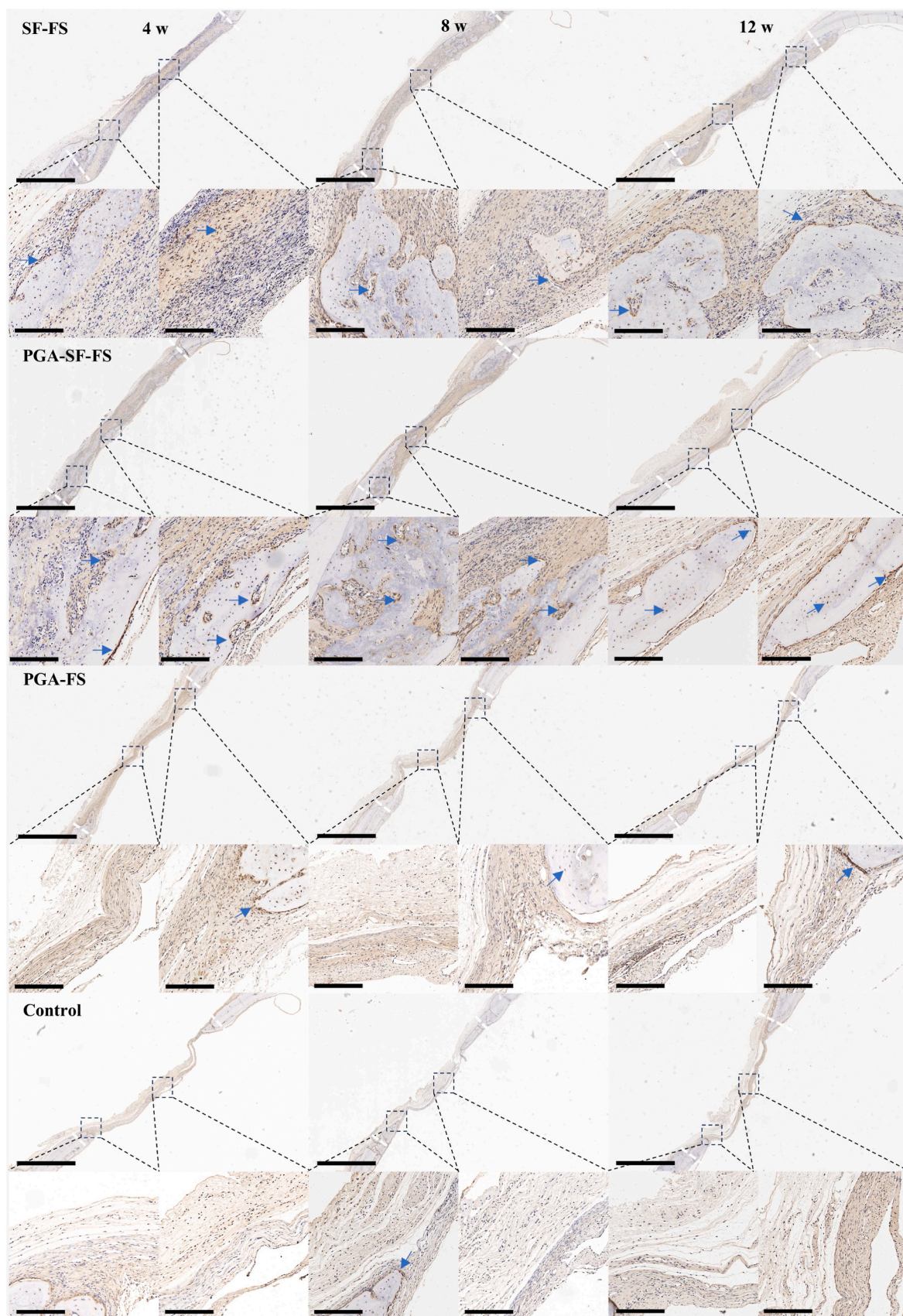
**Fig. 15. Col-1 immunohistochemical staining of SF-FS, PGA-FS, PGA-SF-FS, and control groups implanted in the calvarium defect for 4, 8, and 12 w.** A white dashed line represents the defect margin, and blue arrows represent the Col-1 expression (scale bar: 2 mm for low magnification and 200 μm for high magnification). (For interpretation of the references to colour in this figure legend, the reader is referred to the Web version of this article.)

degradation of PGA. Finally, acidic degradation products of PGA can induce an inflammatory response *in vivo* and autocatalyse the hydrolysis of the PGA matrix [50]. SF is dominated by neutral amino acids, and by combining it with PGA, the pH drop of the degradation solution is reduced, thereby limiting the autocatalytic degradation of PGA [19]. Since the host response of PGA is largely induced by its degradation products [51], the reduction of acidic degradation products of PGA promotes bone healing.

The SBF assay is the classic method for assessing the biological activity of a material. If the material can spontaneously form apatite on the surface after immersion in SBF solution, the material can be considered biologically active and has the potential to promote *in vivo* osseointegration [52]. An ideal bone scaffold material must have the correct chemical composition and proper structure to promote bone growth. The ability to form apatite deposits under physiological conditions is the initiation of the bone regeneration process, and this ability is also a prerequisite for a material considered to have bone regeneration potential. The active apatite layer formed by the reaction between the bioactive scaffold and the physiological fluid is similar to the inorganic phase of bone, providing an adhesive interface between the tissue and the scaffold to obtain a firm bond with bone [53].

The Ca/P ratio of HAp ($Ca_{10}(PO_4)_6(OH)_2$) was $1.68 \pm 0.02$ [52]. The Ca/P ratio of apatite formed on SF-FS and PGA-SF-FS was essentially the same as that of HAp after 28 days of immersion in SBF solution. Enhanced exposure of the $-COO^-$ group of Asp and Glu amino acids of SF electrospinning fibers provides the functional sites for the biomineralization process [54]. It had been reported that premineralized SF scaffolds can increase osteoconductive outcomes, therefore providing an increased osteoconductive environment for BMSCs to regenerate sufficient new bone tissue and confirming that apatite on the surface of SF can promote direct bonding to natural bone tissue *in vivo* [55]. The present study verified that PGA-SF-FS could also mediate the nucleation of apatite like that on SF.

Cell adhesion on the scaffold is considered a prerequisite for subsequent cell proliferation and differentiation [56]. Our results indicated that PGA-SF-FS provided excellent cell adhesion and proliferation properties. SF is similar to collagen in that it is a biopolymer obtained from natural sources containing cell recognition peptides such as RGD (arginine-glycine-aspartic acid), facilitating cell attachment and proliferation [57]. PGA-SF-FS continued the fine bioactivity of SF, thus promoting the adhesion, proliferation, and differentiation of the BMSCs, as determined by the *in vitro* study. BMSCs formed more defined actin stress fibers on PGA-SF-FS, which may be due to the superior tenacity as the cytoskeleton of BMSCs on the tenacious surface had good spreading [58]. However, degradation of the PGA-FS scaffold after 7 days of culture resulted in extensive cell loss and matrix depletion.

One of the keys to bone repair is the differentiation of stem cells into osteoblasts. A tenacious surface has been proven to induce the osteogenic differentiation of MSCs [37], which is consistent with our results. Osteoblastic activity is commonly measured by ALP activity, which is a typical protein product of osteoblast differentiation and phenotype. The increase in ALP activity after 7 and 14 days of culture on SF-FS and PGA-SF-FS suggests the onset of osteogenic differentiation and preparation of the extracellular matrix for mineral deposition. The expression of other bone markers, such as Runx2, Col-1, Osterix, and OCN, confirmed the differentiation of BMSCs on PGA-SF-FS through osteogenic lineage and the formation of mineralized bone tissue. Runx2 and Osterix are crucial for the regulation of genes responsible for the production of bone-specific matrix proteins, including ALP, Col-1, and OCN, and eventually stimulate the mineralization of bone nodules [59]. Col-1 is the main type of collagen found in the bone matrix and a marker of osteoblastic differentiation and bone extracellular matrix formation [56]. The increased expression of OCN in PGA-SF-FS group at 14 days indicated greater osteoblast maturation and matrix mineralization during the onset of nodule formation, which was further confirmed by ARS and quantitative analysis of the calcium nodules at 21 days.

The *in vitro* findings were further supported by a 12-week *in vivo* study of skull defects in SD rat model. The ideal scaffold should be biocompatible, have structural integrity, and act as a temporary framework for the cells until the newly formed bone is generated. In addition, the ideal scaffold should have a proper balance between mechanical properties, a porous architecture [60], and degradability while remaining osteoconductive [53]. According to the *in vivo* results, stepwise degradable PGA-SF-FS with superior tenacity exhibited good osteoconduction, suitable degradation rate, and the ability to promote angiogenesis.

Enhanced mechanical properties and integrity of PGA-SF-FS at an early stage of osteogenesis supported bone formation, which had the highest bone volume fraction and abundant bone trabeculae from 8 weeks. Angiogenesis is a critical element that warrants effective bone regeneration, especially in repairing critical-sized bone defects. It has been suggested that angiogenesis precedes osteogenesis and determines the pattern and efficiency of bone tissue formation during the natural course of fracture healing [61]. This process can be promoted through the active induction of angiogenic growth factor secretion [62]. CD31, known as platelet endothelial cell adhesion molecule-1 (PECAM-1), is a pan endothelial marker with a major role in maintaining endothelial cell barrier function and controlling vascular permeability [63]. Our results showed that CD31 was earlier expressed in PGA-SF-FS groups at the center of the defect, after which it was observed around the new bone and then extending into the bone matrix. Correspondingly, mature bone tissue appeared earlier at the outer edge of the new bone from the results of MT staining, which may confirm the positive effect of early vascularization in the center of the defect on osteogenesis. It suggested a more robust angiogenic response so that nutrients and oxygen reached the inside of the scaffolds more easily. Besides, PGA-SF-FS had a suitable degradation rate, and was almost completely degraded at 12 weeks *in vivo*, which allowed the migration of osteogenic cells to the center of the bone defect. In other words, the degradation and resorption of scaffolds with time matched the remodeling kinetics of host bone tissue. The significant expression of Col-1 observed in the newly formed bone, matrix, lacunae, and scaffold material in the PGA-SF-FS group from 4 to 8 weeks suggests an active role in promoting collagen formation during early bone development. The continued increase in Col-1 expression at 12 weeks, even in the connective tissue surrounding the bone periphery, indicates a sustained influence on bone maturation, which may indicate a favorable microenvironment created by the PGA-SF-FS combination. SF-FS can also induce bone formation; however, the lack of blood vessel in-growth from the host vasculature compromises the viability of a cell-based construct due to insufficient nutrient-waste exchange, hypoxia, and inadequate supply of cytokines and other needful cell types provided by the vascular network [64]. PGA-FS degraded too quickly, and no bone formation was observed at the center of the defect, which emphasized the importance of a proper degradation rate in bone regeneration.

## 5. Conclusion

PGA-SF-FS fabricated using coaxial electrospinning technology exhibited excellent tenacity in wetting regime and demonstrated controlled stepwise degradation characteristics. PGA-SF-FS significantly promoted cell adhesion, proliferation and osteogenic differentiation *in vitro*, and supported vascularization and new bone formation *in vivo*. The controllable degradation behavior, favorable malleability and osteoconductivity of PGA-SF-FS hold great potential as bone grafts and a drug dilivery vehicle in treating bone defects.

## CRediT authorship contribution statement

**Yuan Zhang:** Investigation, Writing – original draft, Visualization, Data curation, Conceptualization.**Yutao Jian:** Supervision, Software, Conceptualization. **Xiao Jiang:** Methodology, Data curation. **Xuerong

**Li:** Visualization, Software. **Xiangnan Wu:** Supervision, Formal analysis. **Juan Zhong:** Validation. **Xiaoshi Jia:** Methodology, Investigation. **Qiulan Li:** Visualization, Data curation. **Xiaodong Wang:** Formal analysis. **Ke Zhao:** Validation, Project administration. **Yitong Yao:** Writing – review & editing, Validation, Conceptualization.

## Declaration of competing interest

The authors declare that they have no known competing financial interests or personal relationships that could have appeared to influence the work reported in this paper.

## Data availability

Data will be made available on request.

## Acknowledgements

## References

[1] X. Zhou, X. Xu, J. Li, D. Hu, T. Hu, W. Yin, Y. Fan, X. Zhang, Oral health in China: from vision to action, Int. J. Oral Sci. 10 (2018) 1–6, https://doi.org/10.1038/s41368-017-0006-6.

[2] S. Titsinides, G. Agrogiannis, T. Karatzas, Bone grafting materials in dentoalveolar reconstruction: a comprehensive review, Jpn. Dent. Sci. Rev. 55 (2019) 26–32, https://doi.org/10.1016/j.jdsr.2018.09.003.

[3] G. Battafarano, M. Rossi, V. De Martino, F. Marampon, L. Borro, A. Secinaro, A. Del Fattore, Strategies for bone regeneration: from graft to tissue engineering, Indian J. Manag. Sci. 22 (2021) 1128, https://doi.org/10.3390/ijms22031128.

[4] V. Petrovic, P. Zivkovic, D. Petrovic, V. Stefanovic, Craniofacial bone tissue engineering, Oral. Surg. Oral. Med. Oral. Pathol. Oral. Radiol. 114 (2012) e1–e9, https://doi.org/10.1016/j.oooo.2012.02.030.

[5] M. Alizadeh-Osgouei, Y. Li, C. Wen, A comprehensive review of biodegradable synthetic polymer-ceramic composites and their manufacture for biomedical applications, Bioact. Mater. 4 (2019) 22–36, https://doi.org/10.1016/j.bioactmat.2018.11.003.

[6] H.J. Haugen, S.P. Lyngstadaas, F. Rossi, G. Perale, Bone grafts: which is the ideal biomaterial? J. Clin. Periodontol. 46 (2019) 92–102, https://doi.org/10.1111/jcpe.13058.

[7] J.R. Fuchs, B.A. Nasseri, J.P. Vacanti, Tissue engineering: a 21st century solution to surgical reconstruction, Ann. Thorac. Surg. 72 (2001) 577–591, https://doi.org/10.1016/s0003-4975(01)02820-x.

[8] J. Yan, J. Li, M.B. Runge, M. Dadsetan, Q. Chen, L. Lu, M.J. Yaszemski, Cross-linking characteristics and mechanical properties of an injectable biomaterial composed of polypropylene fumarate and polycaprolactone co-polymer, J. Biomater. Sci. Polym. Ed. 22 (2011) 489–504, https://doi.org/10.1163/092050610x487765.

[9] S.P. Pilipchuk, A.B. Plonka, A. Monje, A.D. Taut, A. Lanis, B. Kang, W. V. Giannobile, Tissue engineering for bone regeneration and osseointegration in the oral cavity, Dent. Mater. 31 (2015) 317–338, https://doi.org/10.1016/j.dental.2015.01.006.

[10] A. Groetsch, A. Gourrier, D. Casari, J. Schwiedrzik, J.D. Shephard, J. Michler, P. K. Zysset, U. Wolfram, The elasto-plastic nano- and microscale compressive behaviour of rehydrated mineralised collagen fibres, Acta Biomater. 164 (2023) 332–345, https://doi.org/10.1016/j.actbio.2023.03.041.

[11] J. Zhang, S. Yang, X. Yang, Z. Xi, L. Zhao, L. Cen, E. Lu, Y. Yang, Novel fabricating process for porous polyglycolic acid scaffolds by melt-foaming using supercritical carbon dioxide, ACS Biomater. Sci. Eng. 4 (2018) 694–706, https://doi.org/10.1021/acsbiomaterials.7b00692.

[12] C. Shuai, W. Yang, P. Feng, S. Peng, H. Pan, Accelerated degradation of HAP/PLLA bone scaffold by PGA blending facilitates bioactivity and osteoconductivity, Bioact. Mater. 6 (2021) 490–502, https://doi.org/10.1016/j.bioactmat.2020.09.001.

[13] D. Bhattarai, L. Aguilar, C. Park, C. Kim, A review on properties of natural and synthetic based electrospun fibrous materials for bone tissue engineering, Membranes 8 (2018) 62, https://doi.org/10.3390/membranes8030062.

[14] Q. Zhang, J. Fang, W. Liu, Y. Zhao, T. Huang, J. Cui, Y. Yang, Z. Zhou, Synthesis and characterization of poly(d,l-lactide-co-glycolide) modified by maleic

[15] S. Midha, S. Murab, S. Ghosh, Osteogenic signaling on silk-based matrices, Biomaterials 97 (2016) 133–153, https://doi.org/10.1016/j.biomaterials.2016.04.020.

[16] G. Janani, M. Kumar, D. Chouhan, J.C. Moses, A. Gangrade, S. Bhattacharjee, B. B. Mandal, Insight into silk-based biomaterials: from physicochemical attributes to recent biomedical applications, ACS Appl. Bio Mater. 2 (2019) 5460–5491, https://doi.org/10.1021/acsabm.9b00576.

[17] G.H. Altman, F. Diaz, C. Jakuba, T. Calabro, R.L. Horan, J. Chen, H. Lu, J. Richmond, D.L. Kaplan, Silk-based biomaterials, Biomaterials 24 (2003) 401–416, https://doi.org/10.1016/s0142-9612(02)00353-8.

[18] D.N. Rockwood, R.C. Preda, T. Yücel, X. Wang, M.L. Lovett, D.L. Kaplan, Materials fabrication from Bombyx mori silk fibroin, Nat. Protoc. 6 (2011) 1612–1631, https://doi.org/10.1038/nprot.2011.379.

[19] Y. Yao, X. Jia, S. Chen, J. Zhong, X. Wang, Q. Gong, Y. Jian, K. Zhao, Extensive cell seeding densities adaptable SF/PGA electrospinning scaffolds for bone tissue engineering, Biomater. Adv. 137 (2022) 212834, https://doi.org/10.1016/j.bioadv.2022.212834.

[20] J.E. Karbowniczek, K. Berniak, J. Knapczyk-Korczak, G. Williams, J.A. Bryant, N. D. Nikoi, M. Banzhaf, F. de Cogan, U. Stachewicz, Strategies of nanoparticles integration in polymer fibers to achieve antibacterial effect and enhance cell proliferation with collagen production in tissue engineering scaffolds, J. Colloid Interface Sci. 650 (2023) 1371–1381, https://doi.org/10.1016/j.jcis.2023.07.066.

[21] Z. Xie, W.-C. Li, X.-M. Sun, Z.-Y. Lin, L. Ren, Effect of post-treatment on mechanical and biological properties of coaxial electrospun core–shell structured poly(lactic-co-glycolic acid)/gelatin methacrylamide fibrous scaffolds, ACS Appl. Polym. Mater. 4 (2022) 987–998, https://doi.org/10.1021/acsapm.1c01442.

[22] R. Chen, C. Huang, Q. Ke, C. He, H. Wang, X. Mo, Preparation and characterization of coaxial electrospun thermoplastic polyurethane/collagen compound nanofibers for tissue engineering applications, Colloids Surf. B Biointerfaces 79 (2010) 315–325, https://doi.org/10.1016/j.colsurfb.2010.03.043.

[23] S. Mahalingam, R. Matharu, S. Homer-Vanniasinkam, M. Edirisinghe, Current methodologies and approaches for the formation of core–sheath polymer fibers for biomedical applications, Appl. Phys. Rev. 7 (2020) 041302, https://doi.org/10.1063/5.0008310.

[24] G. Cheng, C. Yin, H. Tu, S. Jiang, Q. Wang, X. Zhou, X. Xing, C. Xie, X. Shi, Y. Du, H. Deng, Z. Li, Controlled co-delivery of growth factors through layer-by-layer assembly of core–shell nanofibers for improving bone regeneration, ACS Nano 13 (2019) 6372–6382, https://doi.org/10.1021/acsnano.8b06032.

[25] M.S. Saharudin, R. Atif, I. Shyha, F. Inam, The degradation of mechanical properties in polymer nano-composites exposed to liquid media – a review, RSC Adv. 6 (2016) 1076–1089, https://doi.org/10.1039/c5ra22620a.

[26] M. Erol-Taygun, I. Unalan, M.I.B. Idris, J.F. Mano, A.R. Boccaccini, Bioactive glass-polymer nanocomposites for bone tissue regeneration applications: a review, Adv. Eng. Mater. 21 (2019) 1900287, https://doi.org/10.1002/adem.201900287.

[27] G. Chen, J. Guo, J. Nie, G. Ma, Preparation, characterization, and application of PEO/HA core shell nanofibers based on electric field induced phase separation during electrospinning, Polymer 83 (2016) 12–19, https://doi.org/10.1016/j.polymer.2015.12.002.

[28] V. Catto, S. Farè, I. Cattaneo, M. Figliuzzi, A. Alessandrino, G. Freddi, A. Remuzzi, M.C. Tanzi, Small diameter electrospun silk fibroin vascular grafts: mechanical properties, in vitro biodegradability, and in vivo biocompatibility, Mater. Sci. Eng. C 54 (2015) 101–111, https://doi.org/10.1016/j.msec.2015.05.003.

[29] S. El-Ghazali, H. Kobayashi, M. Khatri, D.-N. Phan, Z. Khatri, S.K. Mahar, S. Kobayashi, I.-S. Kim, Preparation of a cage-type polyglycolic acid/collagen nanofiber blend with improved surface wettability and handling properties for potential biomedical applications, Polymers 13 (2021) 3458, https://doi.org/10.3390/polym13203458.

[30] S. Jiang, Y. Chen, G. Duan, C. Mei, A. Greiner, S. Agarwal, Electrospun nanofiber reinforced composites: a review, Polym. Chem. 9 (2018) 2685–2720, https://doi.org/10.1039/c8py00378e.

[31] Y. Xiao, C. Yang, X. Zhai, L. Zhao, P. Zhao, J. Ruan, D. Chen, D.A. Weitz, K. Liu, Bioinspired tough and strong fibers with hierarchical core–shell structure, Adv. Mater. Interfac. 10 (2022), https://doi.org/10.1002/admi.202201962.

[32] Y. Cheng, L.-D. Koh, D. Li, B. Ji, M.-Y. Han, Y.-W. Zhang, On the strength of β-sheet crystallites of Bombyx mori silk fibroin, J. R. Soc. Interface 11 (2014) 20140305, https://doi.org/10.1098/rsif.2014.0305.

[33] J.R. Porter, T.T. Ruckh, K.C. Popat, Bone tissue engineering: a review in bone biomimetics and drug delivery strategies, Biotechnol. Prog. 25 (2009) 1539–1560, https://doi.org/10.1002/btpr.246.

[34] M.F. Abdullah, T. Nuge, A. Andriyana, B.C. Ang, F. Muhamad, Core–shell fibers: design, roles, and controllable release strategies in tissue engineering and drug delivery, Polymers 11 (2019) 2008, https://doi.org/10.3390/polym11122008.

[35] C. Zhang, D. Song, Q. Lu, X. Hu, D.L. Kaplan, H. Zhu, Flexibility regeneration of silk fibroin in vitro, Biomacromolecules 13 (2012) 2148–2153, https://doi.org/10.1021/bm300541p.

[36] D.E. Discher, Tissue cells feel and respond to the stiffness of their substrate, Science 310 (2005) 1139–1143, https://doi.org/10.1126/science.1116995.

[37] N. Wu, H. Yu, M. Sun, Z. Li, F. Zhao, Y. Ao, H. Chen, Investigation on the structure and mechanical properties of highly tunable elastomeric silk fibroin hydrogels cross-linked by γ-ray radiation, ACS Appl. Bio Mater. 3 (2019) 721–734, https://doi.org/10.1021/acsabm.9b01062.

[38] R. Ravichandran, J.R. Venugopal, S. Sundarrajan, S. Mukherjee, R. Sridhar, S. Ramakrishna, Expression of cardiac proteins in neonatal cardiomyocytes on

PGS/fibrinogen core/shell substrate for cardiac tissue engineering, Int. J. Cardiol. 167 (2013) 1461–1468, https://doi.org/10.1016/j.ijcard.2012.04.045.

[39] B.B. Mandal, S.C. Kundu, Biospinning by silkworms: silk fiber matrices for tissue engineering applications, Acta Biomater. 6 (2010) 360–371, https://doi.org/10.1016/j.actbio.2009.08.035.

[40] J. Zhou, C. Cao, X. Ma, L. Hu, L. Chen, C. Wang, In vitro and in vivo degradation behavior of aqueous-derived electrospun silk fibroin scaffolds, Polym. Degrad. Stabil. 95 (2010) 1679–1685, https://doi.org/10.1016/j.polymdegradstab.2010.05.025.

[41] R.L. Horan, K. Antle, A.L. Collette, Y. Wang, J. Huang, J.E. Moreau, V. Volloch, D. L. Kaplan, G.H. Altman, In vitro degradation of silk fibroin, Biomaterials 26 (2005) 3385–3393, https://doi.org/10.1016/j.biomaterials.2004.09.020.

[42] S. Sharma, S. Bano, A.S. Ghosh, M. Mandal, H.-W. Kim, T. Dey, SubhasC. Kundu, Silk fibroin nanoparticles support in vitro sustained antibiotic release and osteogenesis on titanium surface, Nanomedicine 12 (2016) 1193–1204, https://doi.org/10.1016/j.nano.2015.12.385.

[43] Y.J. Low, A. Andriyana, B.C. Ang, N.I. Zainal Abidin, Bioresorbable and degradable behaviors of PGA : current state and future prospects, Polym. Eng. Sci. 60 (2020) 2657–2675, https://doi.org/10.1002/pen.25508.

[44] Y. Wang, D.D. Rudym, A. Walsh, L. Abrahamsen, H.-J. Kim, H.S. Kim, C. Kirker-Head, D.L. Kaplan, In vivo degradation of three-dimensional silk fibroin scaffolds, Biomaterials 29 (2008) 3415–3428, https://doi.org/10.1016/j.biomaterials.2008.05.002.

[45] L.N. Woodard, M.A. Grunlan, Hydrolytic degradation and erosion of polyester biomaterials, ACS Macro Lett. 7 (2018) 976–982, https://doi.org/10.1021/acsmacrolett.8b00424.

[46] P.K. Samantaray, A. Little, D.M. Haddleton, T. McNally, B. Tan, Z. Sun, W. Huang, Y. Ji, C. Wan, Poly(glycolic acid) (PGA): a versatile building block expanding high performance and sustainable bioplastic applications, Green Chem. 22 (2020) 4055–4081, https://doi.org/10.1039/d0gc01394c.

[47] X.C. Zhang, Science and Principles of Biodegradable and Bioresorbable Medical Polymers: Materials and Properties, Elsevier, United Kingdom, 2016.

[48] N.A. Weir, F.J. Buchanan, J.F. Orr, D.F. Farrar, G.R. Dickson, Degradation of poly-L-lactide. Part 2: increased temperature accelerated degradation, Proc. Inst. Mech. Eng. H 218 (2004) 321–330, https://doi.org/10.1243/0954411041932809.

[49] Y. Yang, X. Chen, Z. Shao, P. Zhou, D. Porter, D.P. Knight, F. Vollrath, Toughness of spider silk at high and low temperatures, Adv. Mater. 17 (2005) 84–88, https://doi.org/10.1002/adma.200400344.

[50] J. Zhang, C. Song, Y. Han, Z. Xi, L. Zhao, L. Cen, Y. Yang, Regulation of inflammatory response to polyglycolic acid scaffolds through incorporation of sodium tripolyphosphate, Eur. Polym. J. 122 (2020) 109349, https://doi.org/10.1016/j.eurpolymj.2019.109349.

[51] W. Liu, Y. Cao, Application of scaffold materials in tissue reconstruction in immunocompetent mammals: our experience and future requirements, Biomaterials 28 (2007) 5078–5086, https://doi.org/10.1016/j.biomaterials.2007.07.028.

[52] T. Kokubo, H. Takadama, How useful is SBF in predicting in vivo bone bioactivity? Biomaterials 27 (2006) 2907–2915, https://doi.org/10.1016/j.biomaterials.2006.01.017.

[53] P. Feng, R. Zhao, W. Tang, F. Yang, H. Tian, S. Peng, H. Pan, C. Shuai, Structural and functional adaptive artificial bone: materials, fabrications, and properties, Adv. Funct. Mater. 33 (2023) 2214726, https://doi.org/10.1002/adfm.202214726.

[54] D. Naskar, A.K. Ghosh, M. Mandal, P. Das, S.K. Nandi, S.C. Kundu, Dual growth factor loaded nonmulberry silk fibroin/carbon nanofiber composite 3D scaffolds for in vitro and in vivo bone regeneration, Biomaterials 136 (2017) 67–85, https://doi.org/10.1016/j.biomaterials.2017.05.014.

[55] J. Zhao, Z. Zhang, S. Wang, X. Sun, X. Zhang, J. Chen, D.L. Kaplan, X. Jiang, Apatite-coated silk fibroin scaffolds to healing mandibular border defects in canines, Bone 45 (2009) 517–527, https://doi.org/10.1016/j.bone.2009.05.026.

[56] J. An, H. Yang, Q. Zhang, C. Liu, J. Zhao, L. Zhang, B. Chen, Natural products for treatment of osteoporosis: the effects and mechanisms on promoting osteoblast-mediated bone formation, Life Sci. 147 (2016) 46–58, https://doi.org/10.1016/j.lfs.2016.01.024.

[57] G. Cheng, J. Dai, J. Dai, H. Wang, S. Chen, Y. liu, X. Liu, X. Li, X. Zhou, H. Deng, Z. Li, Extracellular matrix imitation utilizing nanofibers-embedded biomimetic scaffolds for facilitating cartilage regeneration, Chem. Eng. J. 410 (2021) 128379, https://doi.org/10.1016/j.cej.2020.128379.

[58] M.M. Stevens, Exploring and engineering the cell surface interface, Science 310 (2005) 1135–1138, https://doi.org/10.1126/science.1106587.

[59] E. Hinoi, S. Fujimori, L. Wang, H. Hojo, K. Uno, Y. Yoneda, Nrf2 negatively regulates osteoblast differentiation via Interfering with Runx2-dependent transcriptional activation, J. Biol. Chem. 281 (2006) 18015–18024, https://doi.org/10.1074/jbc.m600603200.

[60] C. Shuai, X. Shi, F. Yang, H. Tian, P. Feng, Oxygen vacancy boosting Fenton reaction in bone scaffold towards fighting bacterial infection, Int. J. Extrem. Manuf. 6 (2023) 015101, https://doi.org/10.1088/2631-7990/ad01fd.

[61] C. Correia, W.L. Grayson, M. Park, D. Hutton, B. Zhou, X.E. Guo, L. Niklason, R. A. Sousa, R.L. Reis, G. Vunjak-Novakovic, In vitro model of vascularized bone: synergizing vascular development and osteogenesis, PLoS One 6 (2011) e28352, https://doi.org/10.1371/journal.pone.0028352.

[62] Y.C. Chai, L.F. Mendes, N. van Gastel, G. Carmeliet, F.P. Luyten, Fine-tuning pro-angiogenic effects of cobalt for simultaneous enhancement of vascular endothelial growth factor secretion and implant neovascularization, Acta Biomater. 72 (2018) 447–460, https://doi.org/10.1016/j.actbio.2018.03.048.

[63] Y. Zhai, K. Schilling, T. Wang, M. El Khatib, S. Vinogradov, E.B. Brown, X. Zhang, Spatiotemporal blood vessel specification at the osteogenesis and angiogenesis interface of biomimetic nanofiber-enabled bone tissue engineering, Biomaterials 276 (2021) 121041, https://doi.org/10.1016/j.biomaterials.2021.121041.

[64] Á.E. Mercado-Pagán, A.M. Stahl, Y. Shanjani, Y. Yang, Vascularization in bone tissue engineering constructs, Ann. Biomed. Eng. 43 (2015) 718–729, https://doi.org/10.1007/s10439-015-1253-3.